Development of in silico airway down to the terminal bronchiole and study of drug delivery efficiency via endotracheal tube

Li, Sixiao
九州大学大学院総合理工学府総合理工学専攻機械・システム理工学メジャー

令　和　５　年　度

修　　士　　論　　文

Development of in silico airway down to the terminal bronchiole and study of drug delivery efficiency via endotracheal tube

九州大学大学院総合理工学府

総合理工学専攻

機械・システム理工学メジャー

伊藤研究室

Li Sixiao

指導教員　　伊藤 一秀（捺印または署名）

提出年月日　令和５年〇〇月〇〇日

CONTENTS

1. Introduction

Lung cancer is a highly lethal disease, responsible for a significant proportion of cancer-related deaths worldwide. It surpasses the combined mortality rates of colon, breast, and prostate cancers(1). Although tumors in the tracheobronchial (TB) tree are rare(2)(3), they exhibit a high malignancy rate, particularly in adults. Surgery and radiation therapy are commonly employed for tumor removal, but they can be invasive and may not be suitable for all patients. Chemotherapy is an alternative treatment method used to eradicate cancer cells, maintain post-treatment health, and prolong survival(4)(5). Among the various chemotherapy approaches, the delivery of chemotherapeutic microparticles through the pulmonary route has shown great performance in combating lung cancer(6)(7). The retention of inhaled drugs in tumor tissue was found to be higher than in healthy tissue, indicating strong anti-tumor effects with minimal side effects. Inhalation delivery of chemotherapeutic agents like interleukin-2 (IL-2) and doxorubicin has shown safety and effectiveness in patients with lung cancer(8)(9). Additionally, inhalation delivery has been found to result in higher drug accumulation in tumors compared to intravenous injection(10). Inhalable nanoparticle drugs containing doxorubicin have also demonstrated improved survival rates in preclinical models(11). Overall, administering chemotherapeutic particles through the pulmonary route holds promise as an effective treatment modality for lung cancer.

While inhalation chemotherapy shows potential in the treatment of lung cancer, it is important to address the potential problem it can cause. Large numbers of particles deposited on healthy tissues can result in side effects to some extent(12). Therefore, an alternative approach to avoid deposition in the upper airway is endotracheal catheter injection. This method involves directly delivering the medication from the trachea into the lower airway by applying an endotracheal tube (ETT), bypassing the upper airway where deposition is undesired(13)(14).

The ETT is a medical device that plays a crucial role in the field of air supply and critical care medicine. Its development can be traced back to the early 19^{th} century when efforts were made to secure the airway during surgical procedures(15). The ETT is a flexible tube inserted into the trachea through the mouth or nose, providing a direct pathway for the delivery of oxygen and anesthetic gases to the lungs, as

well as facilitating the removal of carbon dioxide. The primary function of the ETT is to ensure adequate ventilation and oxygenation of the patient(16). It allows for precise control of the airflow, enabling the anesthetist or healthcare provider to regulate the depth and rate of respiration during surgery or in critical care settings(17). It is also utilized in emergency medicine to manage patients with respiratory distress or failure, providing immediate air support(18). Additionally, the ETT serves as a conduit for the administration of medication, such as insulin delivery, pain management, cancer therapy, and nano-therapeutics(19)(20). ETTs are typically constructed from medical-grade materials such as polyvinyl chloride (PVC), silicone, or Teflon. PVC is commonly utilized in disposable catheters due to its cost-effectiveness and ease of sterilization. Silicone, on the other hand, is a popular choice for reusable catheters due to its flexibility and biocompatibility.

By employing ETT to release particles downstream from the trachea, deposition in the upper airway can be avoided. While catheters have been explored in other human body parts, such as the urinary route(21) and the central venous route(22), for cancer treatment, the feasibility of using an ETT for the delivery of chemotherapeutic particles to lung tumors has not been extensively studied.

Determining the feasibility of drug delivery using the ETT for tumor treatment requires an understanding of how chemotherapeutic particles interact with pulmonary airflow and deposit in lung airways. Conducting high-resolution, quantitative in vitro or in vivo studies to obtain detailed dynamics of these interactions can be challenging due to limitations in imaging resolution, flexibility, and ethical considerations. Computational fluid particle dynamics (CFPD) offers an alternative approach to predicting air-particle flow dynamics in the lungs(19)(23). For decades, CFPD has been used to enhance our understanding of respiratory drug delivery mechanisms by providing physics-based computational models that can save time and resources compared to traditional experimental models. One CFPD study introduced a novel inhalation therapy using short-pulsed bolus aerosolized drug particles, which achieved high drug delivery efficiency to small airways(24). While there are also some CFPD studies examining particle trajectories and airflow patterns in airways with lung tumors, some research has explored the impact of tumor size and ventilatory characteristics on regional flow behavior to aid targeted drug delivery(25)(26).

However, there were few CFPD studies focused on the detailed particle deposition in the whole human lower airway by using ETT.

Therefore, to fill in this gap, by applying an ETT, particle deposition characteristics in the human lower airway were analyzed. The results can serve as a reference to the tumor treatment in terms of chemotherapy.

In addition, since it has been proven that the lungs of severe patients are inadequate to deliver oxygen and conduct air exchange, mechanical ventilators (MV) play an important role in air support(27). In terms of ventilator waveform processes, conventional mechanical ventilators(CMV) can be divided into different types, such as pressure-time waveform, flow-time waveform, volume-time waveform, and pressure-volume loop(28). The selection of the waveform is adjusted based on the clinical objectives, the specific needs of the patient, and the availability of the waveform on the ventilator. However, CMV can exert a certain degree of ventilator-induced lung injury (VILI) due to the mechanized expansion and contraction of the human lung(29). First and foremost, CMV, due to the presence of respiratory cycles, may impose high-pressure points on the lungs. However, not every individual's lungs can adapt to these high-pressure points. Short-term usage may not significantly impact the lungs, but for patients requiring prolonged medical intervention, extended use of traditional ventilators can potentially lead to lung injury. Furthermore, the application of traditional ventilators relies on the assumption that the lungs possess a certain degree of elasticity, allowing them to expand and contract normally under pressure. However, for patients with severe medical conditions or pathological lung damage, their lungs may struggle to undergo normal expansion and contraction, rendering traditional ventilators less suitable. In order to address the aforementioned issues associated with traditional ventilators, this study also developed a new type of static ventilator which is friendlier to the human lung. The static ventilator can keep the human lung in a constant volume all the time by importing and exporting airflow with the same flow rates. This study, by analyzing the ventilation efficiency in the lower airway, also provided a reference to the development of the static ventilator.

2. Methodology

2.1 Geometry development

The human respiratory tract is a complex anatomical structure that plays a crucial role in the exchange of gases between the body and the external environment. It can be broadly divided into two main parts: the upper airway and the lower airway. The upper respiratory tract encompasses the nasal cavity, pharynx, and larynx, while the lower respiratory tract comprises the trachea, bronchi, bronchioles, and the delicate alveoli within the lungs. This intricate system ensures the delivery of oxygen to the bloodstream and the removal of carbon dioxide from the body, which is essential for sustaining life and maintaining physiological balance. Starting with the upper airway, the journey of inhaled air begins with the nasal cavity. The nasal cavity, being the entry point of the air, serves several crucial functions. It acts as a natural filter, trapping airborne particles, dust, and potentially harmful pathogens before they can enter the lower airway. Additionally, the nasal cavity conditions the inhaled air, adjusting its temperature and humidity to protect the delicate lung tissues from extreme environmental conditions. Moving further down, the air passes through the pharynx, a shared passage for both the respiratory and digestive systems. From here, it enters the larynx, often referred to as the "voice box." The larynx plays a vital role in vocalization, housing the vocal cords that vibrate to produce sound during speech.

The lower respiratory tract commences at the trachea, a sturdy, cartilaginous tube that serves as the main pathway for air transport into the lungs. The trachea further divides into the left and right main bronchi, marking the first generation of the lower airway. These main bronchi, in turn, lead to the secondary bronchi, followed by tertiary bronchi, bronchioles, and eventually the terminal bronchioles. The branching pattern of the lower airway results in an intricate network of air passages that progressively diminish in size. As air travels deeper into the lungs, the bronchi and bronchioles become narrower, culminating in the terminal bronchioles. The terminal bronchioles represent the 16^{th} generation of the airway, and beyond this point, the respiratory pathway bifurcates into the respiratory bronchioles, alveolar ducts, and alveolar sacs, collectively known as the acinus. These delicate structures are responsible for

facilitating gas exchange with the bloodstream, where oxygen is absorbed and carbon dioxide is released. An essential characteristic of the lower airway is its extensive branching, resulting in a total of 23 airway generations. Each generation represents a bifurcation into smaller air passages, contributing to a vast surface area for efficient gas exchange. The intricate structure of the lower airway maximizes contact between the inhaled air and the alveolar membrane, optimizing the exchange of oxygen and carbon dioxide between the lungs and the blood(30). Fig.2.1.1 shows the division of airway generations.

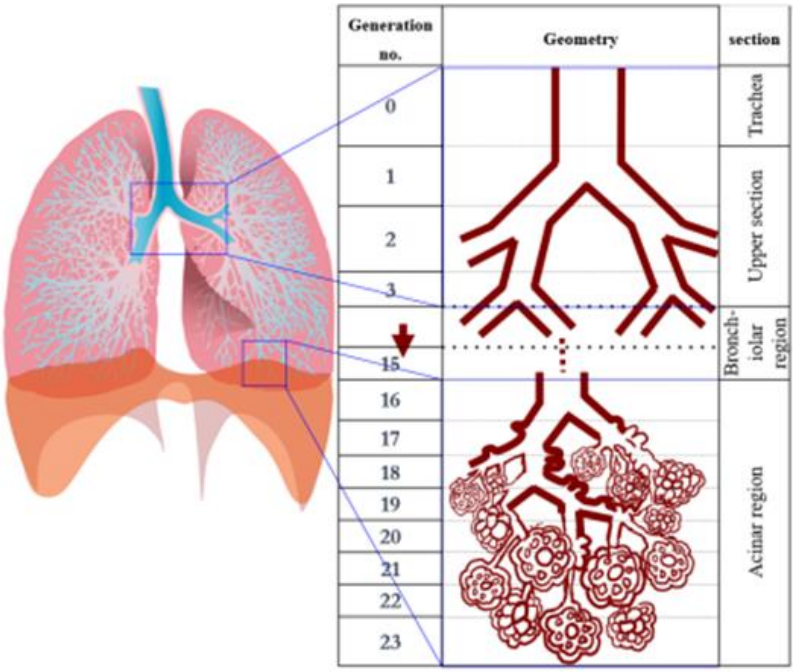

Fig.2.1.1 Human lower respiratory tract classification

A 59-year-old male's respiratory tract was segmented from CT images using a spatial resolution of 0.625 mm on the x- and y-axis and 0.5 mm on the z-axis. Mimic software was used for semi-automated and manual segmentation of the lower respiratory tract from the trachea to the 8th generation. Fig.2.1.2 shows the human lower airway model from tracheal to 8th generation generated from Mimic software. To get the lower airway model from the trachea to the 16th generation, artificial bronchial models from the 9th to the 16th generation need to be generated. The parameters of the artificial bronchial models were calculated using Weibel's work(31). Fig.2.1.3, regarding the 10th generation as an example, shows the

principle of artificial airway model development. Eq.1-3 are the governing equations to calculate the sizes of artificial airway models. Then, SpaceClaim software was applied to create the artificial airway models, before which the artificial airway models were manually connected to the real model. Finally, an ETT was inserted at the position of the trachea for drug delivery. Fig.2.1.4 shows the intubated lung model and the structure of ETT. Then, the intubated lung model was used in this study to analyze the drug delivery to treat the lung tumor. It is noticeable that for the lower airway, this study used the same model as a previous autonomous respiratory study(23).

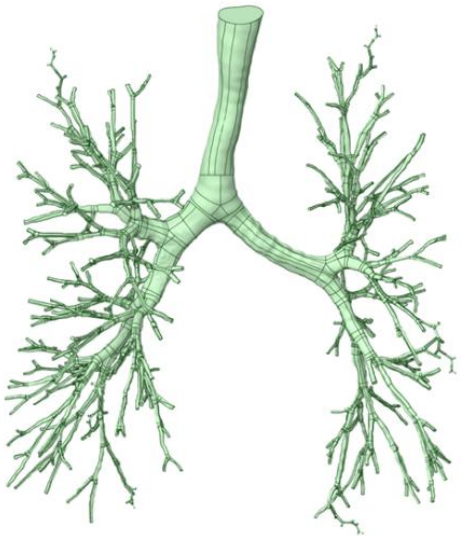

Fig.2.1.2 Lower airway model from the trachea to 8th generation

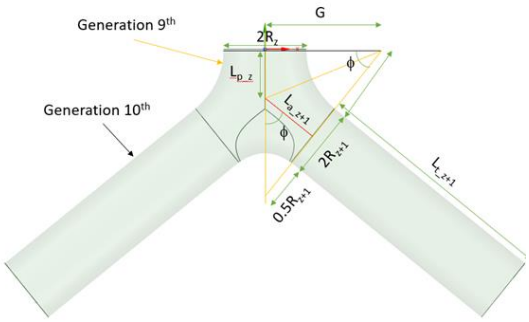

Fig.2.1.3 The principle of artificial model development

$$L_z = L_{p\_n} + L_{a\_n} + L_{t\_n} \tag{1}$$

$$L_{p\_n} = G_n \tan \phi_n - \frac{{}^{G_n}/_{\cos \phi_n} - (G_n - R_n + R_{n+1})}{\sin \phi_n} \tag{2}$$

$$L_{a\_n} = \frac{G_n(1-\cos \phi_n) + (R_{n-1} - R_n)}{\sin \phi_n} \cos \phi_n \tag{3}$$

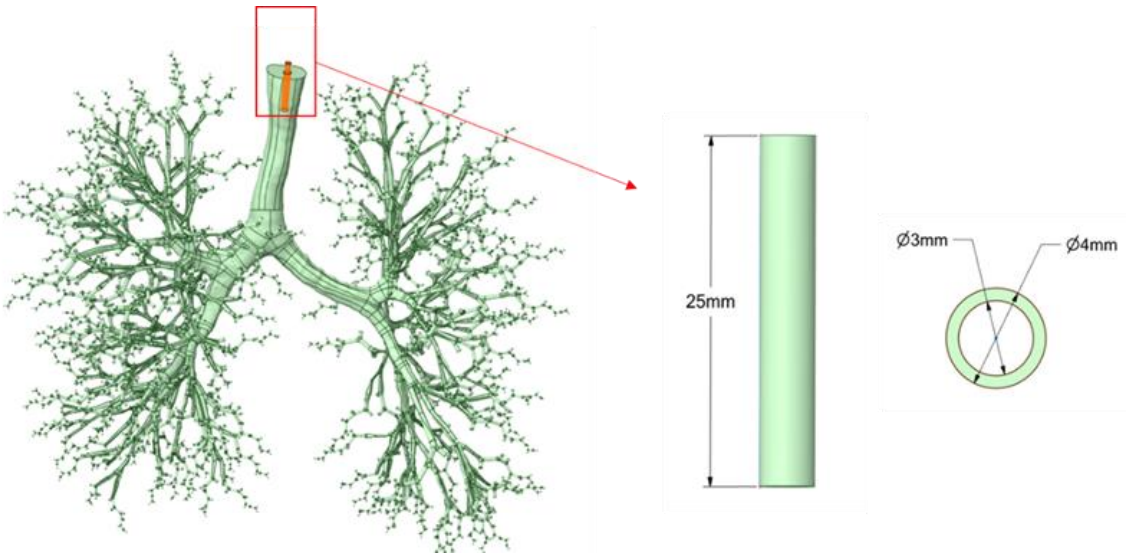

Fig.2.1.4 The intubated lung model and the structure of ETT

Fig.2.1.5 shows the segmentation process of the lower airway from CT images and Fig.2.1.6 shows the representative of a truncated artificial bronchial tube from 9th to 16th generation. Through the combination of the real model from CT and artificial model from Spaceclaim, the lower airway model was successfully developed. Fig.2.1.7 shows the model applied in the autonomous respiratory study, in which five parts are included: anterior airway, nasopharynx, oral cavity, larynx, and lower airway.

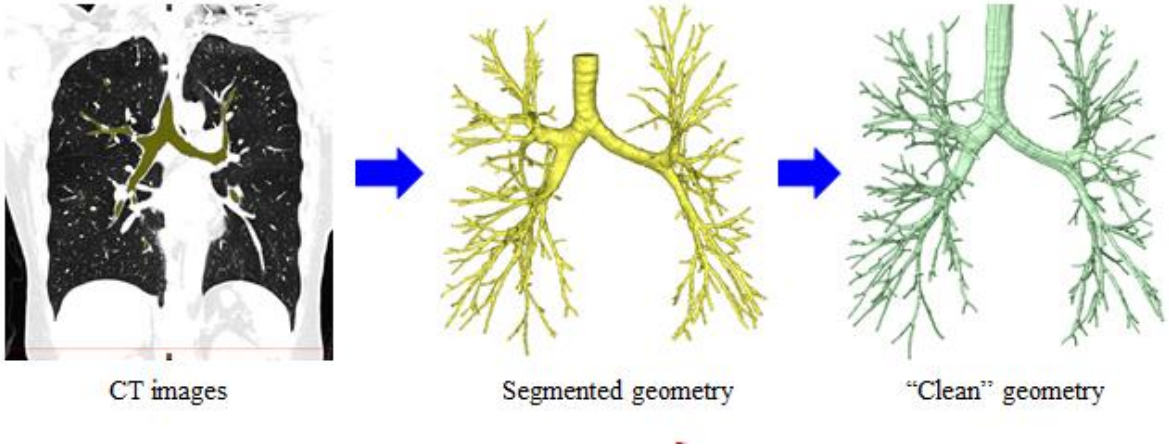

Fig.2.1.5 Segmentation process of the lower airway from CT images

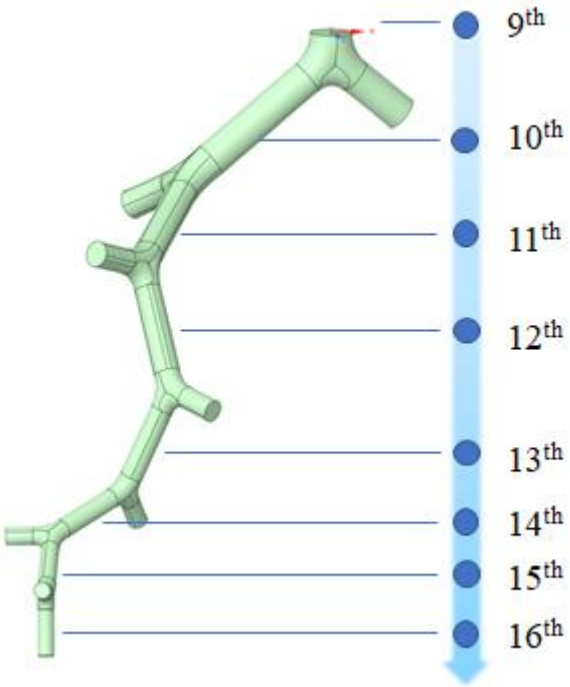

Fig.2.1.6 Representative of a truncated artificial bronchial tube from the 9-16th generation

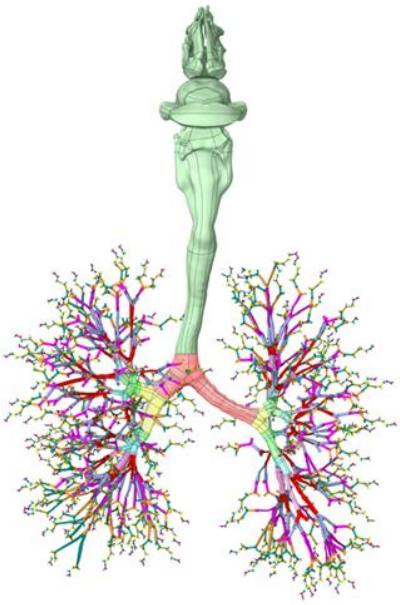

Fig.2.1.5 The model of the autonomous respiratory study

For the model of the static ventilator, the lower airway model remained, while the ETT was replaced with a newly designed ETT, which is shown in Fig.2.1.6. There were two tubes in the newly designed ETT, including the inner tube and the outer tube. The inner tube has a diameter of 3mm and a length of 15mm, while the outer tube has an outer diameter of 7mm and an inner diameter of 4mm, with a length of 25mm. By applying this ETT, simultaneous air import and export can be realized.

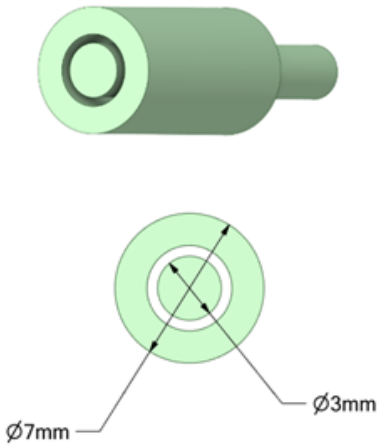

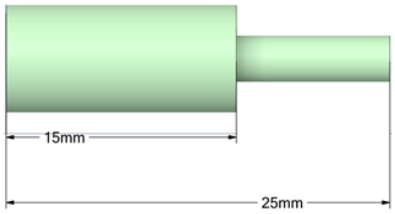

Fig.2.1.6 The new ETT applied in the static ventilator

2.2 Grid design

The domains of interest were discretized and meshed using poly hex-core elements. Ten prism layers with a first height of 10μm were applied in the trachea. Five prism layers with a first height of 5μm were applied to the ETT and each generation of the bronchial tubes. Fig.2.2.1 shows the mesh design in the trachea area. The final mesh elements were counted to be approximately 30 million cells for the entire model. An optimal number of grids is indispensable in any CFD study to balance the computational cost and accuracy of the simulation results, which can be obtained via a grid independence test. Despite the heavy mesh design used in this study for the lower airway, the fluid characteristics were found to be predominantly laminar. Therefore, a suitable grid size was applied to each bronchial generation, corresponding to its diameter. The grid designs in the lower airway tract were completely the same in the ETT drug delivery study, static ventilator study, and autonomous respiratory study.

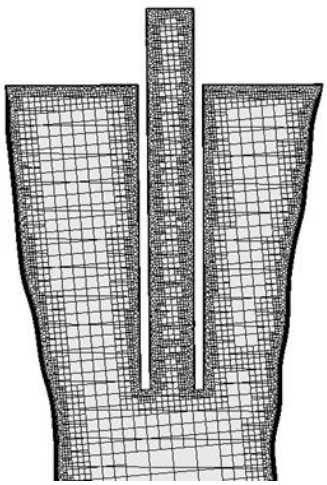

(a)

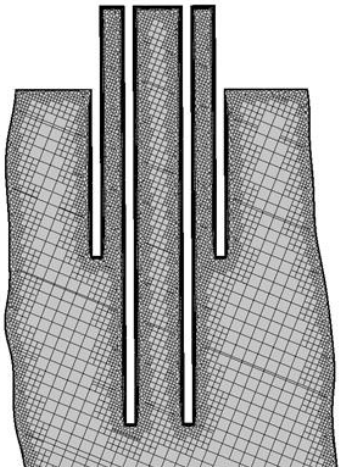

(b)

Fig.2.2.1 (a) The meshing of drug delivery study in the trachea area (b) The meshing of the static ventilator in the trachea area

2.3 Boundary conditions of the ETT drug delivery study

For the velocity boundary condition at the trachea inlet, a non-uniform boundary condition was set, with the airflow rate of 7.5L/min. The non-uniform velocity profile was determined based on the velocity profile at the same plane of the autonomous respiratory study. Fig.2.3.1 shows the airflow inlet of the trachea. Fig.2.3.2 shows the velocity profiles at the same plane of the drug delivery study and the autonomous respiratory study. For the velocity boundary condition of the ETT, three velocities were set. In Case 1, the average velocity of the trachea inlet (0.5m/s) was chosen. Then, to analyze the effect of the injection velocity on the particle deposition, 1m/s, and 2m/s were set in Cases 2 and 3. The Reynolds number in the three cases was respectively 100, 200, and 400, which meant the airflow could be regarded to be incompressible. The detailed velocity boundary conditions are shown in Fig.2.3.3.

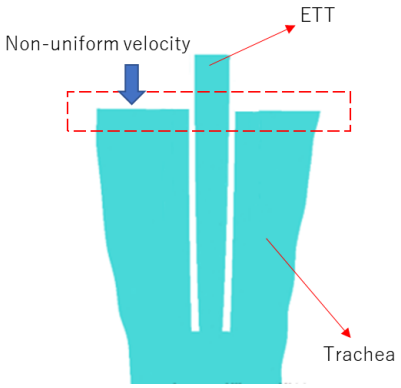

Fig.2.3.1 The configuration around the inlet area

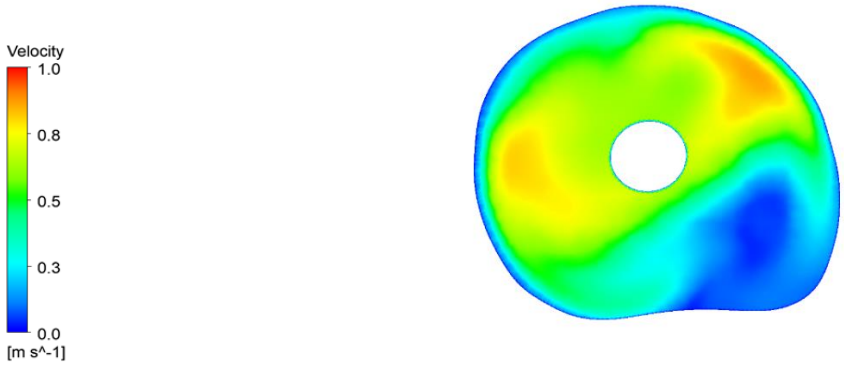

(a)

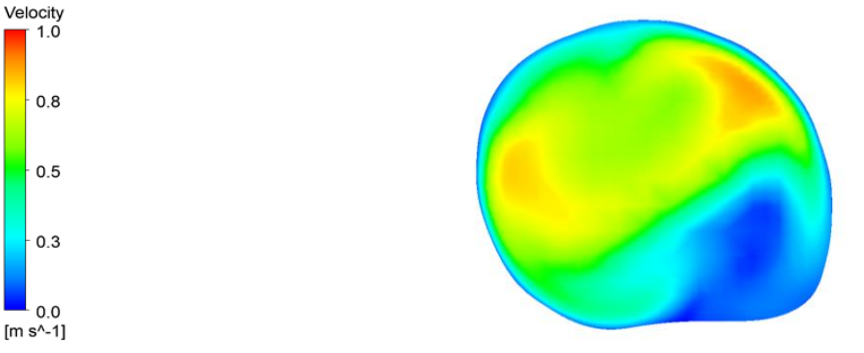

(b)

Figure 2.3.2 (a) The velocity boundary condition at the trachea inlet under the ETT drug delivery study (b) the velocity profile at the same plane under the autonomous respiratory study

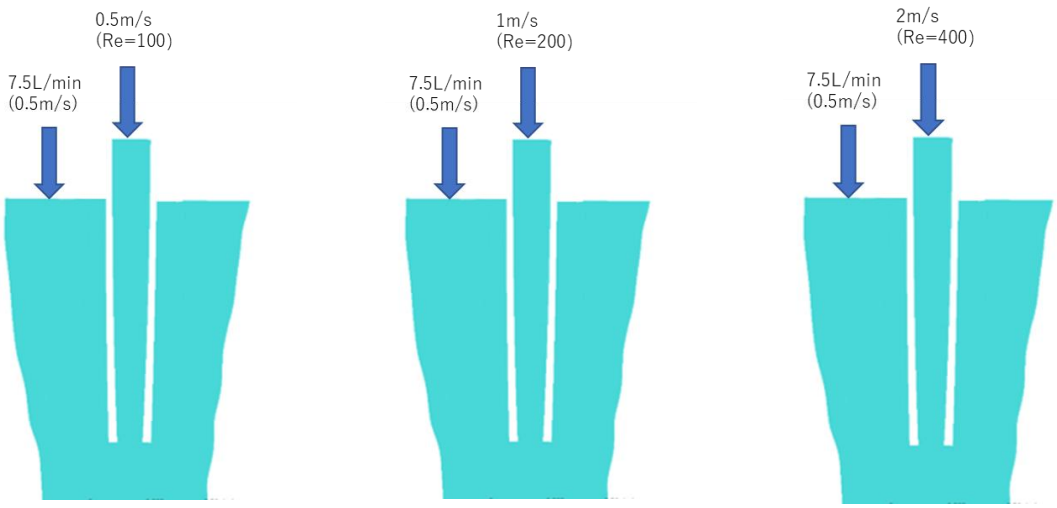

Case 1 Case 2 Case 3

Fig.2.3.3 Various inlet velocity boundary conditions of the ETT drug delivery study

For temperature boundary conditions, the non-uniform temperature profile was applied as the boundary condition at the trachea inlet by the same method as the velocity boundary condition. Fig.2.3.4 shows the temperature profile at the same plane as the ETT drug delivery study and the autonomous respiratory study. The walls of the respiratory tract were set to be 310 K, also the same as the autonomous respiratory study. The ETT was set to be adiabatic, which means there is no heat flux between the air and the ETT. The air temperature at the ETT inlet was set to be the average temperature of the air at the trachea inlet (309.8K). The detailed temperature boundary condition is shown in Fig.2.3.5.

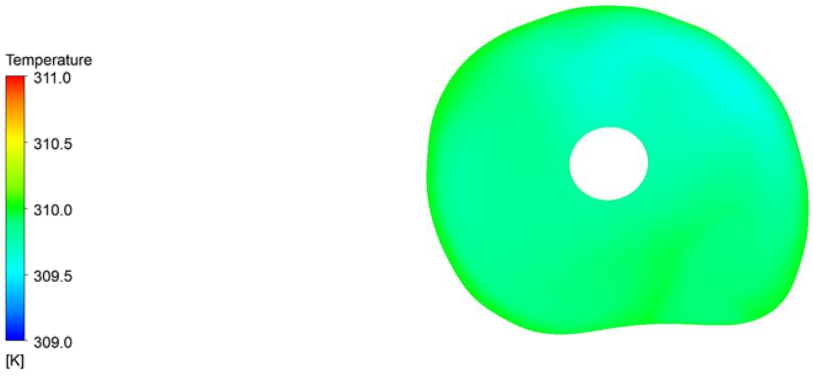

(a)

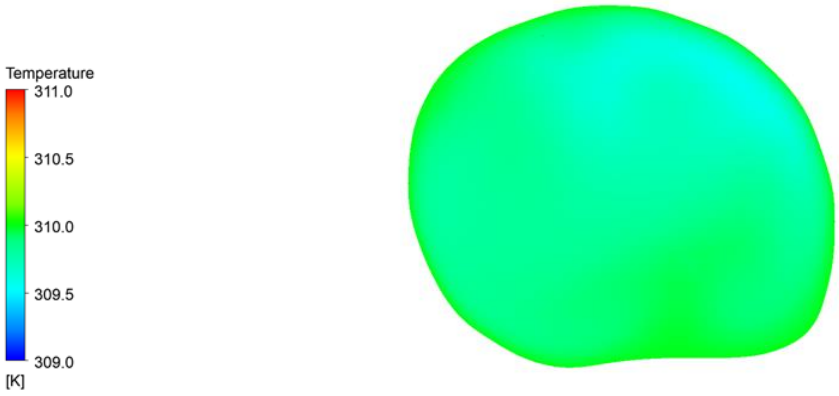

(b)

Figure 2.3.4 (a) The temperature boundary condition at the trachea inlet under the ETT drug delivery study (b) the temperature profile at the same plane under the autonomous respiratory study

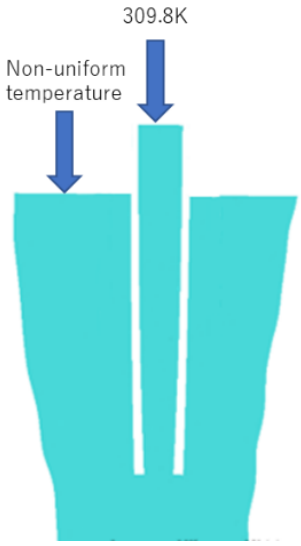

Fig.2.3.5 The inlet temperature boundary condition of the ETT drug delivery study

For the turbulence boundary conditions, non-uniform turbulent kinetic energy and turbulent dissipation rate were also set using the same method with velocity and temperature profiles at the trachea inlet. Turbulent intensity at the ETT inlet was set to be 10% which was the same as the autonomous

respiratory study. Based on the structure of the ETT, the hydraulic diameter at the endotracheal tube inlet was set to be 0.003m.

For the outlet boundary condition, this study also shared the same boundary condition with the autonomous respiratory study. Outflow weighting was applied as the boundary condition for all the outlets, in which the different lung lobes would have different ventilation rates, which can be estimated based on the percentage of lung height from the basal regions(32). The estimated ventilation airflow rates for each lung lobe are listed in Table 1 and used to assign flow weighting values to the corresponding outlets. Thus, the sum of the flow weighting values of all outlets belonging to the same lung lobe equals the corresponding value. Table 1 reveals that the right lower lobe (RLL) has the highest ventilation rate, accounting for approximately 30% of the total ventilation. Moreover, the right lung has a higher overall ventilation rate (around 53%) compared to the left lung (around 47%). This observation was consistent with previous studies that have reported a bias toward the right lung's ventilation rate(33)(34).

Table 1. The ventilation airflow rate of each lung lobe

Lung lobe	Ventilation airflow rate (%)
Right upper lobe-RUL	0.1192
Right middle lobe-RML	0.1087
Right lower lobe-RLL	0.3000
Left upper lobe-LUL	0.2374
Left lower lobe-LLL	0.2347

Particles with diameters ranging from 0.002 μm to 10 μm were imported from the ETT in sequence. The same as the autonomous respiratory study, monodisperse ultrafine-to-coarse particles with a density equal to that of pure water, that is, 1000kg/m^3, were chosen. The walls of the lower airway were set in perfect trap condition, while ETT as perfect reflect condition. All the outlets were set to be the escape

condition. Altogether, 50000 particles were injected in each case for each separate particle aerodynamic diameter. Fig.2.3.6 shows the particle injection position of the ETT drug delivery study.

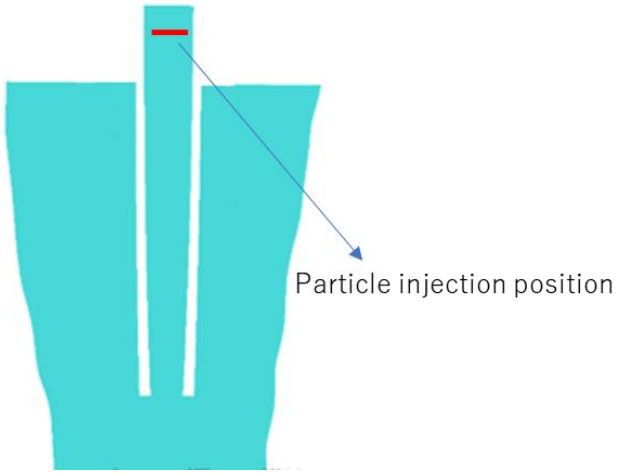

Fig.2.3.6 Particle injection position of the ETT drug delivery study

The complete boundary conditions of the ETT drug delivery study and the autonomous respiratory study are shown in Table 2.

Table 2. Total boundary conditions of the ETT study and autonomous respiratory study

Parameter	ETT drug delivery study	Autonomous respiratory study
Simulation domain	From the trachea to the 16th generation of the lower airway	From the nasal cavity to the 16th generation of the lower airway
Inflow flowrate	$Q_{trachea}$= 7.5L/min (non-uniform) $Q_{injection}$= 0.2, 0.4, and 0.8L/min (0.5, 1, 2m/s)	Q= 7.5L/min
Inflow temperature	$T_{trachea\ airflow}$= 309.8K (non-uniform) $T_{ETT\ airflow}$: 309.8K	$T_{nasal\ cavity\ airlow}$ = 293K
Inflow turbulence	$TKE_{trachea}$: non-uniform $TDR_{trachea}$: non-uniform Turbulence intensity$_{ETT}$=10%	Turbulence intensity$_{inlet}$=10%

	Hydraulic diameter$_{ETT}$=0.003m	
Outlet	Continuous phase: outflow weighting Discrete phase: escape	Continuous phase: outflow weighting Discrete phase: escape
Respiratory tract wall	Velocity: no slip T = 310K Discrete phase: perfect trap	Velocity: no slip T = 310K Discrete phase: perfect trap
ETT wall	Velocity: no slip Heat Flux$_{ETT}$: 0W/m^2 Discrete phase: perfect reflect	
Discrete phase	Particle number: 50000 Density: 1000kg/m^3 Injection location: ETT	Particle number: 50000 Density: 1000kg/m^3 Injection location: nasal cavity

2.4 Boundary conditions of static ventilator

For the ventilator development, five air-supplying/exhausting configurations were assumed for the ETT, as shown in Fig.2.4.1. Case 1 served as a simulation of the autonomous respiratory condition, in which fresh air was supplied through the inner tube (red arrow) and the outlets of the model were the same as Chapter 2.3. In Case 2, the inlet boundary condition remained, while the outer tube worked as the outlet. It should be noted that the supplying/exhausting flow rates in Case 2 were identically set at 1 L/min. In Case 3, the functions of the inner and outer tubes were reversed; specifically, the air was supplied through the outer tube, and the inner tubes acted as the exhausting component. In Cases 4 and 5, the supplying/exhausting configurations were maintained the same as in Cases 2 and 3, respectively; however, a higher flow rate of 10 L/min was assumed. All the boundaries of the model, except for the ETT, were set to walls from Case 2 to Case 5. For the other boundary conditions, the same parameters were chosen as in

Chapter 2.3. Besides, it should be noted that the boundary conditions of Cases 3 and 5 are currently used in MV.

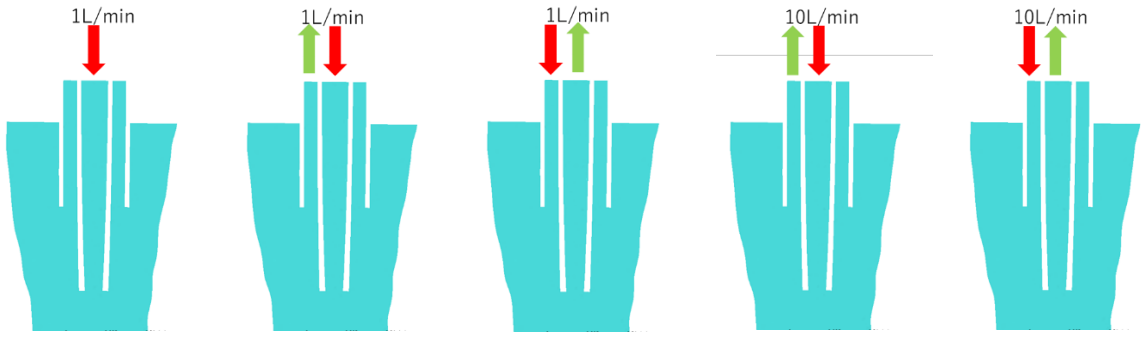

Fig.2.4.1 Boundary conditions of the five cases

2.5 Numerical simulation of airflow pattern

To model the continuous flow of an incompressible fluid in the human respiratory system, the computational method was used to solve what is known as the Reynolds-averaged Navier-Stokes (RANS) equations. This allows a steady-state solution for the fluid flow within the respiratory tract.

$$\frac{\partial \bar{U}_i}{\partial X_i} = 0 \tag{4}$$

$$\frac{\partial \bar{U}_i}{\partial t} + \frac{\partial}{\partial x_j}\left(\bar{U}_i \bar{U}_j\right) = -\frac{1}{\rho_g}\frac{\partial \overline{p_g}}{\partial x_i} + v\frac{\partial^2 \bar{U}_i}{\partial x_j^2} - \frac{\partial}{\partial x_j}\left(\overline{u_i' u_j'}\right) \tag{5}$$

where $\bar{U}$ and u' mean the mean velocity and the fluctuating components, and p_g, ρ_g, and v indicate the pressure, density, and viscosity of the fluid, respectively. The term Reynolds stresses, $-\overline{u_i' u_j'}$, states the closure problem to the RANS equation. The eddy viscosity turbulence model provides a relationship between the Reynolds stresses and the mean velocity gradient tensor.

$$-\overline{u_i' u_j'} = v_T\left(\frac{\partial \bar{U}_i}{\partial x_j} + \frac{\partial \bar{U}_j}{\partial x_i}\right) - \frac{2}{3}k\delta_{ij} \tag{6}$$

where k is the average kinetic energy, δ_{ij} is the Kronecker delta, and v_T is the eddy viscosity.

For the turbulence model, the study utilized the low-Reynolds-type k-ε as it has been proven effective in accurately predicting flow characteristics within the human airway(35). The model's ability to

incorporate a damping function in the near-wall region makes it particularly useful for analyzing the viscous sublayer at wall surfaces. Additionally, this model has been shown to produce highly precise results in particle deposition analyses(36)(37).

2.6 Numerical simulation of the discrete phase

To determine the transport and deposition characteristics of ultrafine-to-coarse particles in the respiratory tract, the Fluent software (ANSYS, Inc.) was employed to calculate particle trajectories using the discrete phase model. The Lagrangian equation was solved to track the movement of particles, with acting body forces utilized in the prediction process. First, the airflow field was solved as part of the continuous phase, after which the Lagrangian discrete phase was computed to determine the paths of individual particles, as shown in Eq.7:

$$\frac{d\vec{u}_p}{dt} = \vec{F}_D + \vec{F}_G + \vec{F}_S + \vec{F}_B \tag{7}$$

where the subscript ρ refers to the particle phase; $\vec{F}_D$ is the drag force per unit particle mass, derived from Strokes drag law, defined as shown in Eq.8:

$$\vec{F}_D = \frac{18\mu}{\rho_p d_a^2 C_c}\frac{C_D Re_p}{24}(\vec{u} - \vec{u}_p) \tag{8}$$

where μ is the air viscosity, $\vec{u}$ is the fluid flow velocity, $\vec{u}_p$ is the particle velocity, d_a is the aerodynamic particle diameter, ρ_p is the particle density, C_D is the drag coefficient, Re_p is the particle Reynolds number, and C_c is the Cunningham correction factor for Stokes' drag law which is calculated from Eq.9:

$$C_c = 1 + \frac{\lambda}{d_a}(2.34 + 1.05e^{-0.39^{d_a}/\lambda}) \tag{9}$$

where λ is the mean free path of air molecule.

$\vec{F}_G$, the second term, indicates gravitational settling. $\vec{F}_S$ (Eq.10), the third term, is the Saffman's lift force due to shear on a unit mass basis.

$$\vec{F}_S = \frac{5.188\nu^{1/2}\rho d_{ij}}{\rho_p d_a (d_{lk}d_{kl})} \tag{10}$$

For the fourth term, $\vec{F}_B$ is the Brownian force expressed by Eq.11:

$$\vec{F}_B = \xi\sqrt{\frac{216\mu k_B T_{air}}{\pi d_a^5 \rho_p^2 C_c \Delta t}} \tag{11}$$

where ξ is the unit variance independent Gaussian random number, k_B is the Stefan-Boltzmann constant, T_{air} is the absolute temperature of the inhaled air, and Δt is the particle integration time step. To include the impact of Brownian motion on the movement and settling of ultrafine particles of various sizes, a custom-made software program that incorporates a user-defined function (UDF) was utilized. This allows for more precise modelling of how the particles are transported and deposited. Afterwards, the discrete particle model was utilized to trace the particles.

In this study, the total deposition efficiency (DE) and regional DE were calculated based on the ratio of the number of particles deposited to the total number of particles imported, as shown in Eq.12

$$\eta_a = \frac{C_{deposited-lower-airway}}{C_{imported-via-ETT}} \times 100\% \tag{12}$$

where $C_{deposited-\text{total}}$ is the number of particles deposited in total, $C_{imported-\text{via-ETT}}$ is the number of particles imported from ETT.

Accordingly, the local DE in the region i can be calculated using the same expression Eq.13

$$\eta_b = \frac{C_{i-deposited}}{C_{imported-via-ETT}} \times 100\% \tag{13}$$

For the autonomous case, Eq.14 and 15 are used to calculate DE in the lower airway and regional DE

$$\eta_c = \frac{C_{deposited-lower-airway}}{C_{\text{entering-lower-airway}}} \times 100\% \tag{14}$$

$$\eta_{\text{d}} = \frac{C_{i-deposited}}{C_{\text{entering-lower-airway}}} \times 100\% \tag{15}$$

Besides, the penetration efficiency (PE) in the i region can be estimated using the ratio of particles that escape the filtration effects of its upstream region and the total number of particles inhaled through the nostrils (Eq.16)

$$\eta_{\text{e}} = \frac{C_{\text{entering-via-inlet}} - C_{\text{upstream-deposited}}}{C_{\text{entering-via-inlet}}} \times 100\% \tag{16}$$

where $C_{upstream-deposited}$ is the number of particles deposited in the upstream regions corresponding to region i. The inlet indicates the ETT tube and nasal cavity for ETT cases and autonomous case, respectively.

2.7 Numerical simulation of the age of air

Ventilation efficiency is the mean assessment criteria for the performance of the static ventilator. On the basis of the spatial distribution of tracer concentration, the SVE3, which was proposed by Ref.(38), as shown in Eq. 14 and 15, was calculated here as the index for the local ventilation efficiency.

$$SVE3(X) = \frac{C(X)}{C_s} \tag{14}$$

$$C_s = \frac{q_0 V}{Q} \tag{15}$$

$C(X)$ is the concentration at point X, while C_s is the concentration under the perfectly mixed condition, Q is the inhalation flow rate, and V is the total volume of the ETT-lung model with a value of 6.712×10-5 m3.

3. Results and discussion

3.1 Airflow field of the ETT drug delivery study

There are three cases included in the ETT drug delivery study in total. In the three cases, the initial velocities in the ETT were different (0.5m/s, 1m/s, and 2m/s, respectively) while the airflow rates in the trachea inlet remained consistent. The flow field patterns in the human lower airway of 0.5m/s Case are shown in Fig. 3.1.1. Fig. 3.1.1a shows the streamline of the airflow. The incoming airstreams into the lower region of the respiratory system underwent initial bifurcation at the first branching point, leading to the subsequent separation of the flow into two distinct airstreams directed towards the left and right lungs. The intricate network of bronchial airways further facilitated the continuous division of the flow at the carina ridges, resulting in a complex branching pattern until the 16th generation was reached. Overall, the velocity magnitude within the lower airway segment was relatively subdued; nevertheless, localized regions exhibited notable fluid acceleration. Fig.3.1.1b shows the fluid region with a velocity magnitude＞ 1m/s via volume distribution. The high-velocity fluid flow can be seen at the 1^{st} and 2^{nd} bifurcations. Then, some velocity accelerations can be seen in some random positions in different generations. It is noticeable that most of the velocity accelerations took place in the lung lobes of RML, RLL, and LLL. It is because of the different ventilation rates in each lung lobe, which is shown in Table.1. Fig.3.1.1c shows the overlap of the high-velocity fluid flow and the domain of the generations of 5^{th}, 6^{th}, and 7^{th}, from which a great overlap effect can be seen in 6^{th} and 7^{th} generations. Fig.3.1.1d shows the airflow characteristic in the trachea area. Since the average velocity of the trachea inlet was determined as the velocity in ETT, no velocity jump exists in the trachea area.

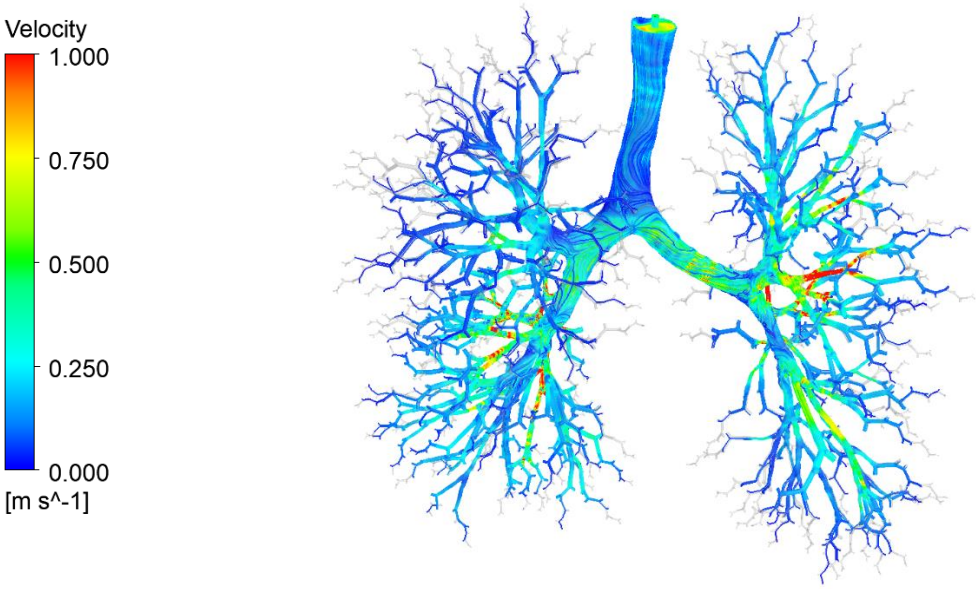

(a)

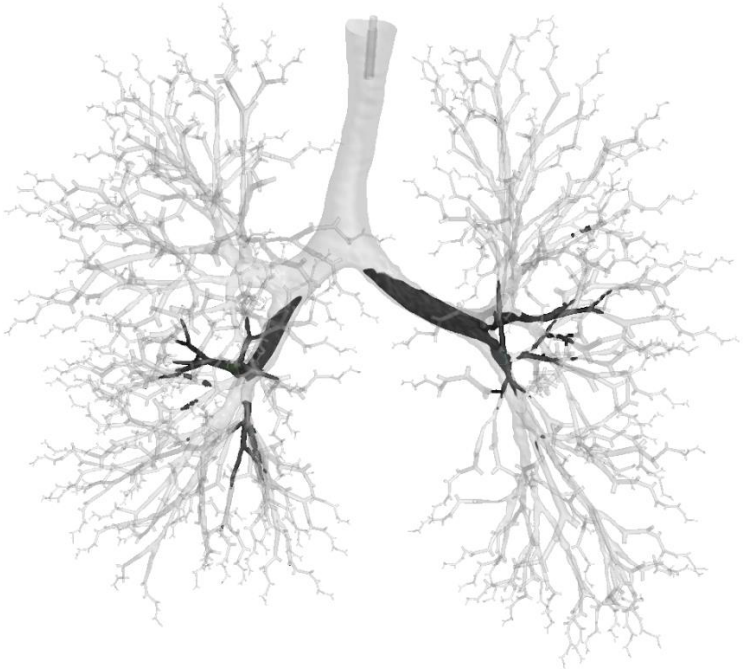

(b)

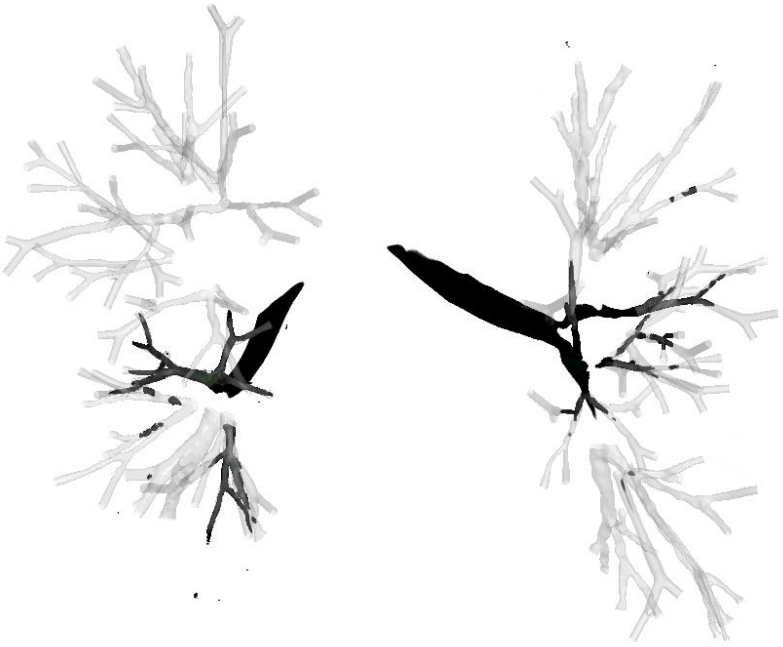

(c)

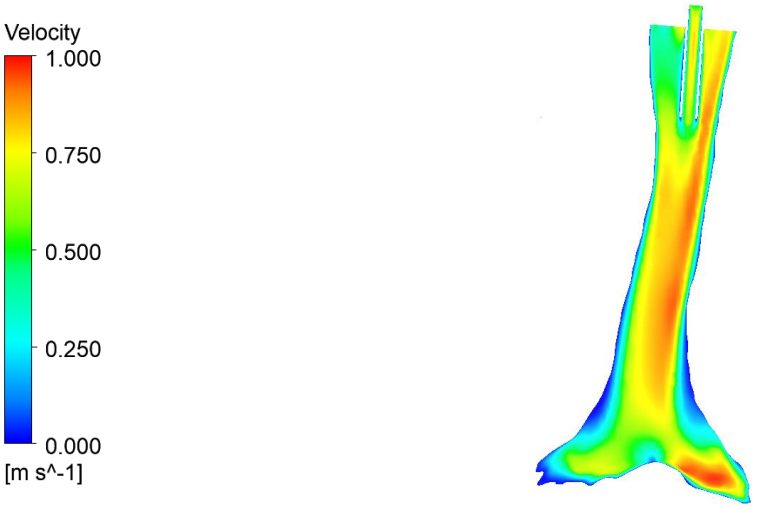

(d)

Fig.3.1.1 The flow field distribution in the human lower airway of Case 1 (a) Airflow streamline. (b) The volume distribution of high-velocity flow (＞1m/s) in the lower airway. (c) The overlap effect of the high-velocity flow (＞1m/s) and the domain of the generations of 5^{th}, 6^{th}, and 7^{th}. (d) Airflow characteristic in the trachea area.

Fig.3.1.2 shows the flow field distribution of Case 2. Fig.3.1.2c displays the overlap of high-velocity flow (＞1m/s) with the domain of 5th, 6th, and 7th. The overlap effect in the domain indicated that velocity accelerations were mainly located in the domain of 5th, 6th. Fig.3.1.1d shows the airflow characteristic in the trachea area as a result of the velocity difference between ETT and trachea inlet, a jet flow in the ETT area can be seen, although it was not obvious.

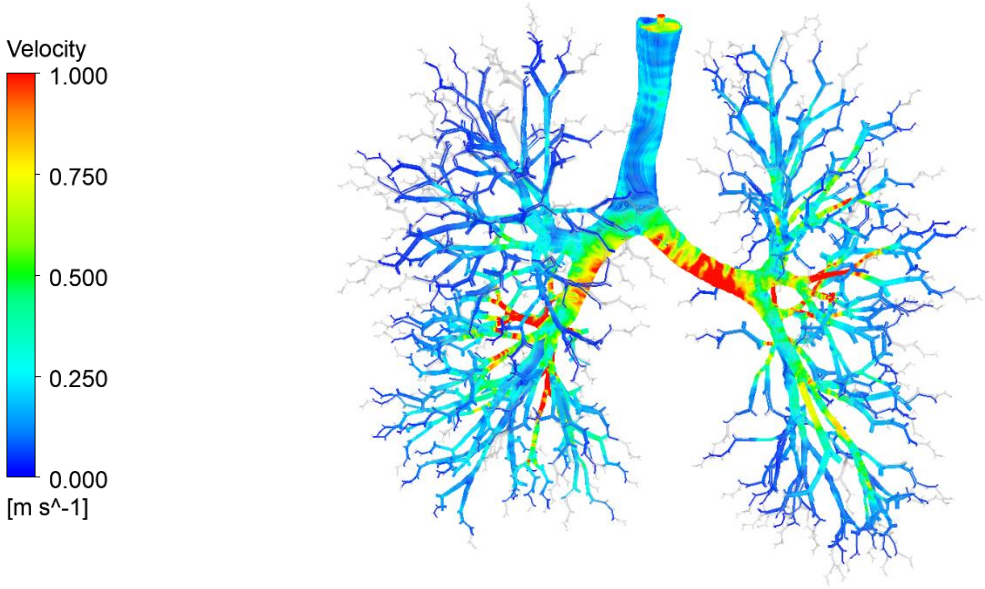

(a)

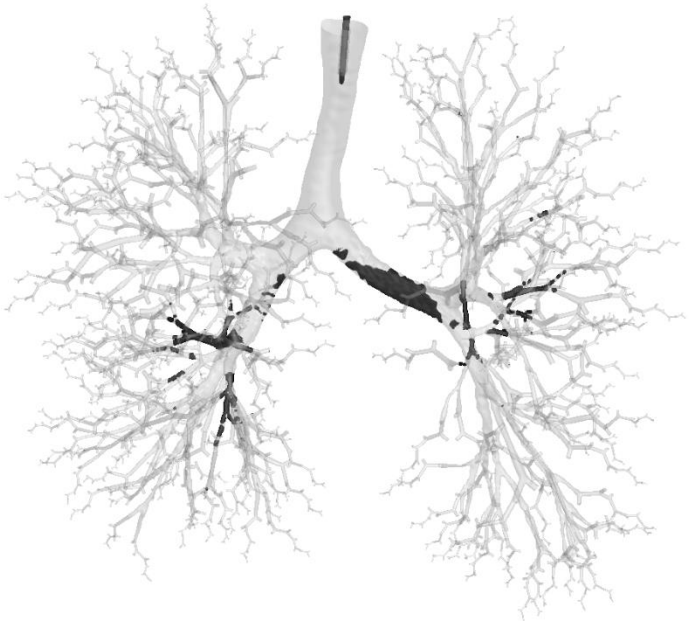

(b)

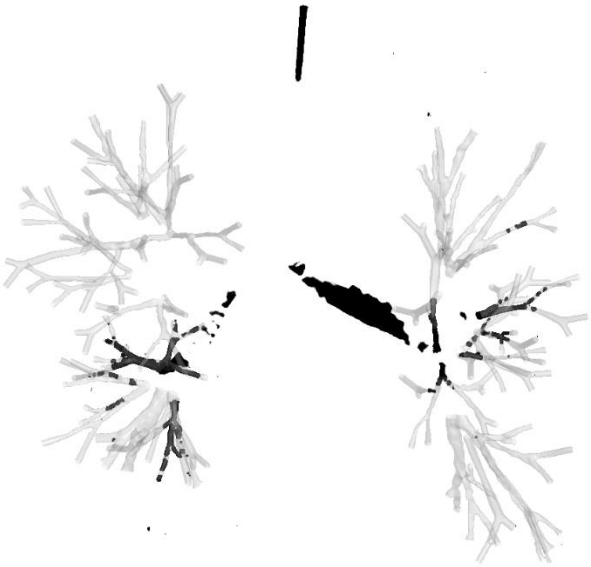

(c)

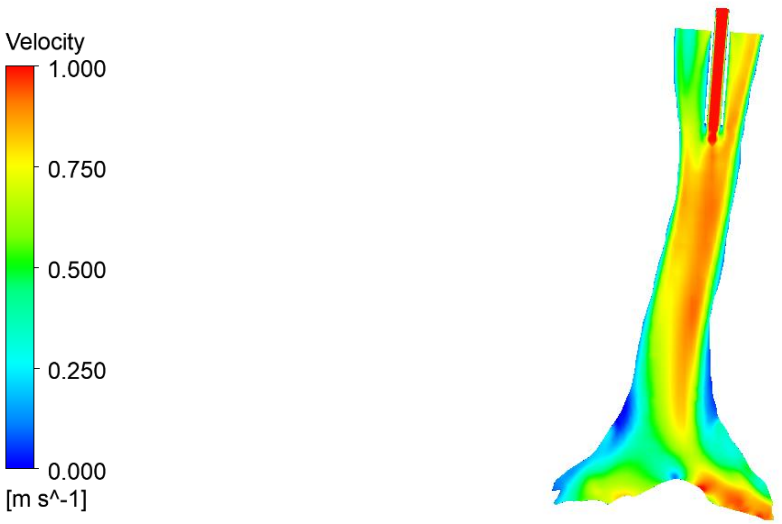

(d)

Fig.3.1.2 The flow field distribution in the human lower airway of Case 2 (a) Airflow streamline. (b) The volume distribution of high-velocity flow (＞1m/s) in the lower airway. (c) The overlap effect of the high-velocity flow (＞1m/s) and the domain of the generations of 5th, 6th, and 7th. (d) Airflow characteristic in the trachea area.

Fig.3.1.3 shows the flow field distribution of Case 3. By comparing Fig.3.1.1b, Fig.3.1.2b, and Fig.3.1.3b, it can be noticed that as the ETT initial velocity increased, more high-velocity (＞1m/s) area can be seen in the human lower airway, especially in the trachea, 1st and 2nd generations. However, when it turns to Fig.3.1.3c, similar velocity acceleration characteristics can be seen in Fig.3.1.2c in 5th and 6th generations since there was a great velocity difference between the trachea inlet (0.5m/s) and ETT (2m/s), an obvious jet flow can be seen in the trachea. After entering the trachea, the jet collided with the 1st generation airway, subsequently bifurcating and distributing the flow into the left and right lung lobes.

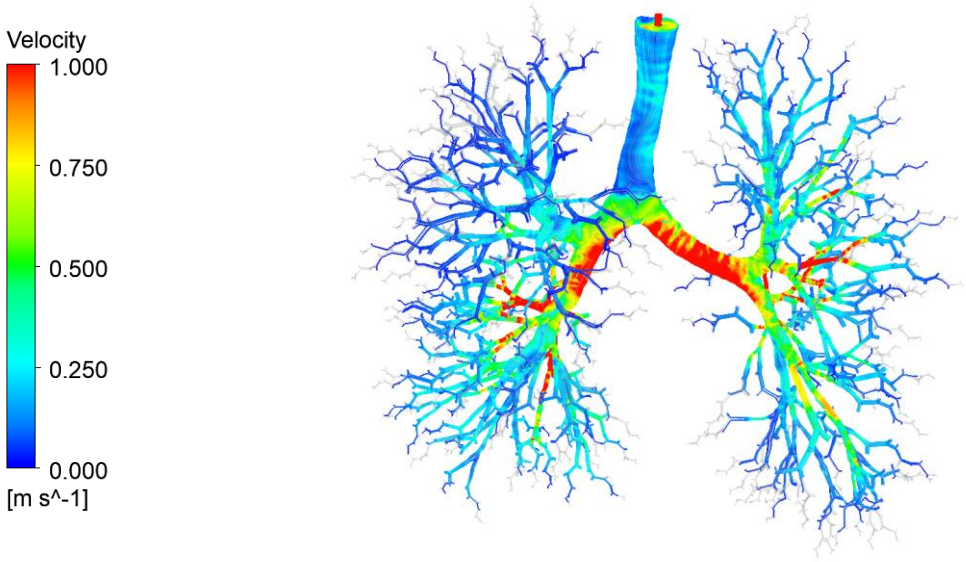

(a)

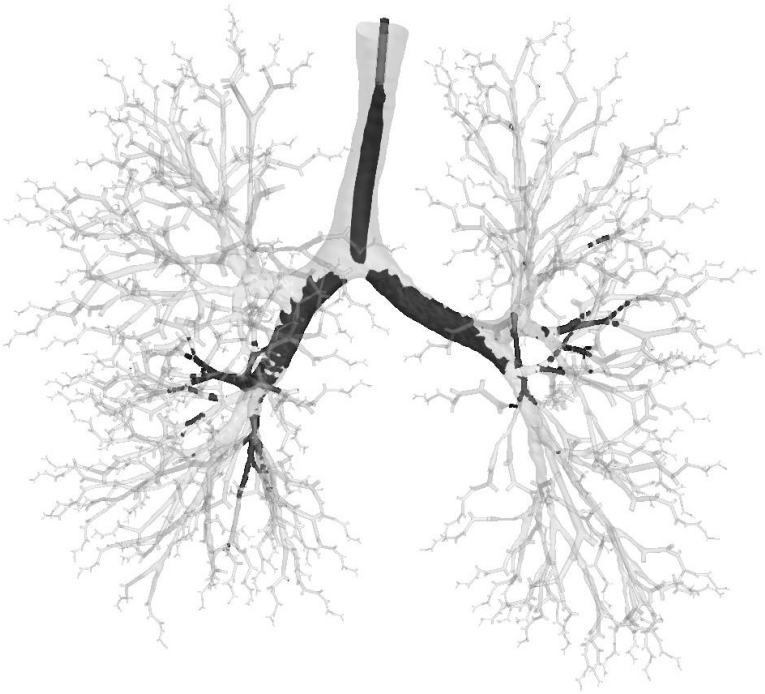

(b)

(c)

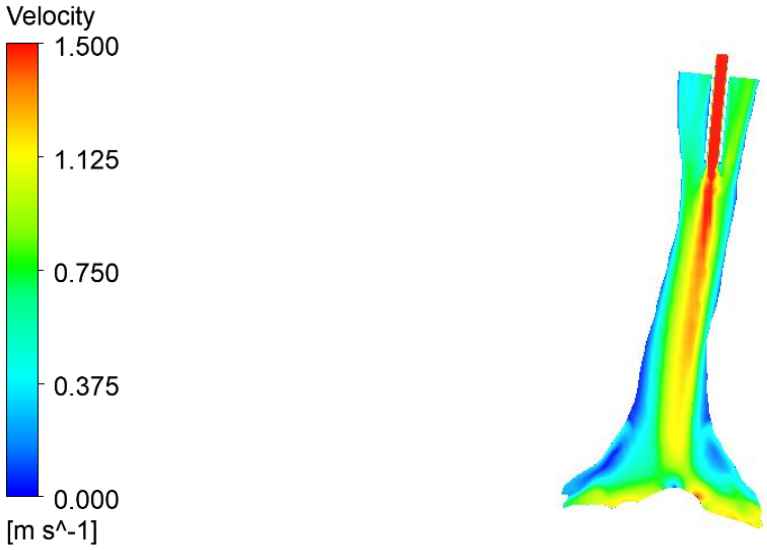

(d)

Fig.3.1.3 The flow field distribution in the human lower airway of Case 3 (a) Airflow streamline. (b) The volume distribution of high-velocity flow (＞1m/s) in the lower airway. (c) The overlap effect of the high-velocity flow (＞1m/s) and the domain of the generations of 5th, 6th, and 7th. (d) Airflow characteristics in the trachea area.

3.2 Deposition efficiency analysis of the ETT drug delivery study

3.2.1 Deposition efficiency analysis and comparison with autonomous respiratory study

Table 3 illustrates the sedimentation mechanisms for particles of different sizes. For ultrafine and fine particles, their primary deposition mechanism is diffusion settling. As particle size decreases, the Brownian motion becomes more pronounced, leading to a stronger diffusion settling effect and higher deposition efficiency. In contrast, for coarse particles, the dominant deposition mechanism is inertial settling. As particle diameter increases, the flow velocity becomes faster, resulting in a higher deposition efficiency for these larger particles.

Table 3. Deposition mechanisms of different particle sizes

Ultrafine particle	Diffusion deposition
Fine particle	Diffusion deposition
Coarse particle	Inertial deposition

The results of DE in the human lower respiratory tract are exhibited in Fig.3.2.1.1, which were calculated by Eq.12 and 14. The figure shows the DE of the three ETT cases and the autonomous respiratory cases with particle diameters from 0.002 μm to 10μm. Fifty thousand particles with a density of 1000kg/m^3 were imported from the ETT and nasal cavity, respectively. Because the autonomous respiratory case was well validated with previous datasets of measurements(39)(40) and numerical simulations(41)(42)(43)(44)(45), this study, through the comparison with the autonomous case, to confirm the reliability of the ETT cases. In the case of ultrafine particles (< 0.1 μm), almost all the particles with a diameter of 0.002 μm were deposited in the domain, before which DE sharply reduced as the particle size approached 0.1 μm, which is consistent with the autonomous respiratory case. In the range of 0.1 – 2.5 μm, DE was found to be relatively low (< 10%), while in terms of coarse particles, DE rapidly increased proportionally with the particle size, with the same trend as the autonomous respiratory case. The different deposition mechanisms for particles of varying diameters contribute to this phenomenon. For ultrafine and fine particles, diffusion deposition driven by Brownian motion is the primary mechanism. However, the intensity of Brownian motion decreases with increasing particle diameter, resulting in lower DE for larger particles. For particles with a diameter of 0.002μm, their high Brownian motion intensity leads to nearly complete deposition within the control domain. For coarse particles, deposition is mainly governed by inertial forces resulting from gravity. As the particle diameter increases, so does the gravitational force, leading to stronger inertial forces. Consequently, the DE of coarse particles increases along with the diameter. Since the same simulation method was used in the ETT cases and autonomous respiratory case, and consistent DE trends among the cases were shown, the simulation results of the ETT cases are relatively reliable. Table.4 shows the specific particle deposition values of the four cases, which are

corresponding to Fig.3.2.1.1. Table.5 shows the detailed particle delivery in the autonomous case. Table.5 demonstrates that in the autonomous respiratory case, as particle size increases, particle deposition in the upper airway initially decreases and then increases. Conversely, the number of particles entering the lower airway increases initially and then decreases. Additionally, the total deposition in the lower airway shows a fluctuating pattern, which can be attributed to variations in the total number of particles entering the lower airway for different particle sizes. Furthermore, the application of the aforementioned particle deposition mechanisms can effectively explain the data presented in Table.5.

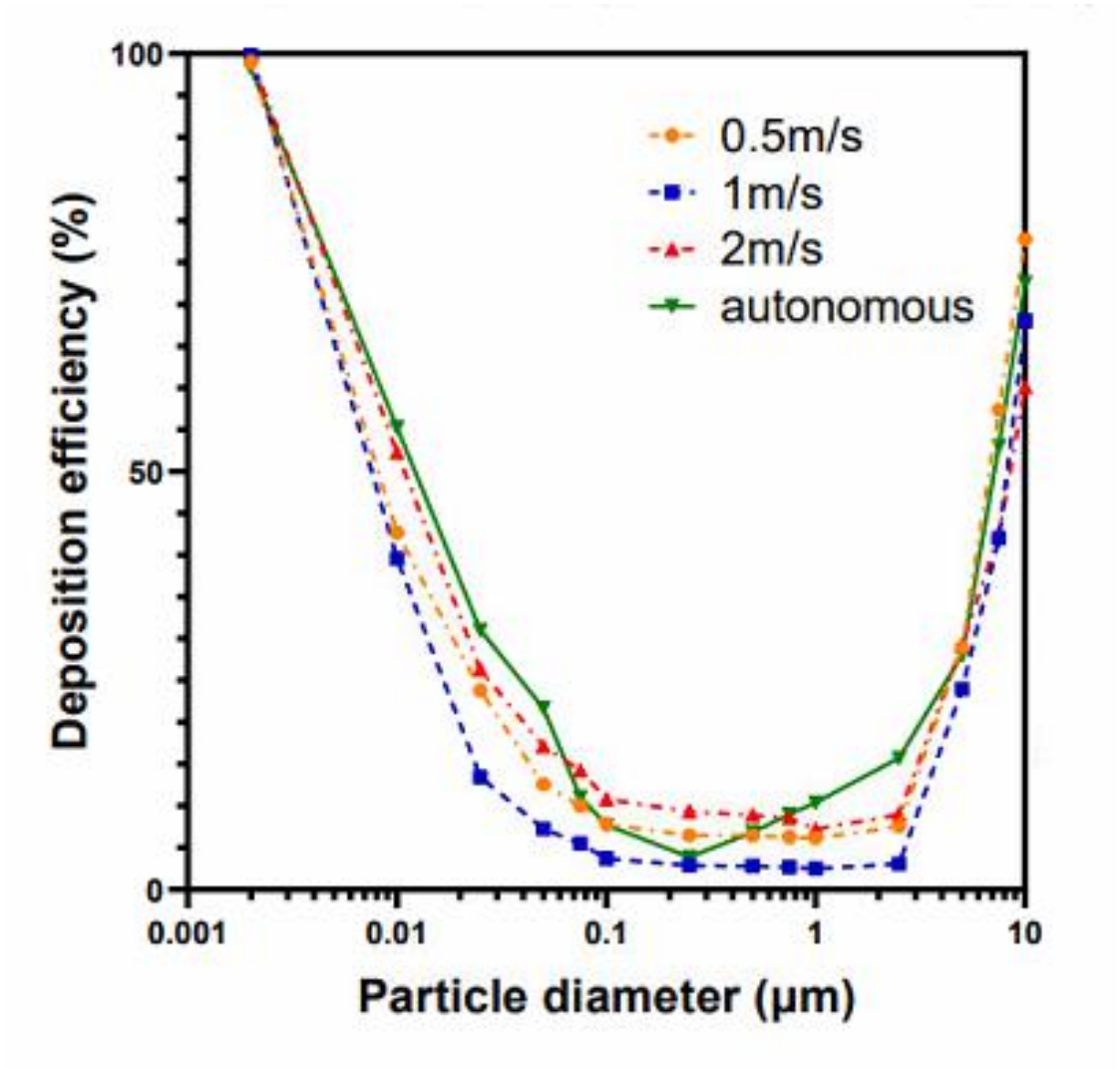

Fig.3.2.1.1 Deposition efficiencies in the lower airway of ETT cases and autonomous respiratory case

Table 4. Total particle depositions in the lower airway in the ETT cases and autonomous case

Particle diameter (μm)	0.5m/s	1m/s	2m/s	Autonomous
0.002	49918	49898	49893	8430
0.01	21339	19795	26150	19165
0.025	11921	6715	13147	13020
0.05	6289	3622	8569	9600
0.075	5002	2745	7115	5150
0.1	3901	1845	5424	3675
0.25	3257	1442	4678	1885
0.5	3223	1405	4464	3290
0.75	3134	1350	4280	4310
1	3074	1263	3601	4960
2.5	3770	1542	3645	7280
5	14511	12016	14602	12315
7.5	28726	21096	21310	22640
10	38891	34019	30080	30215

Table 5. Detailed particle delivery in the autonomous case

Particle diameter (μm)	Enter upper airway	Upper airway deposition	Enter lower airway	Lower airway deposition
0.002	50000	41256	8744	8430
0.01	50000	15468	34532	19165
0.025	50000	13250	36750	13020

0.05	50000	11789	38211	9600
0.075	50000	3754	46246	5150
0.1	50000	2513	47487	3675
0.25	50000	1578	48422	1885
0.5	50000	1745	48255	3290
0.75	50000	2564	47436	4310
1	50000	2613	47387	4960
2.5	50000	3978	46022	7280
5	50000	5546	44454	12315
7.5	50000	7548	42452	22640
10	50000	8546	41454	30215

Fig.3.2.1.2 shows the particle delivery ratios in the right and left lung with particle diameters of 0.01μm, 0.1μm, 0.5μm, 5μm, and 10μm under three ETT cases, respectively. From Fig.3.2.1.2, it can be observed that for the ETT velocity of 0.5m/s, the particle delivery ratio in the right lung was approximately 60% for different particle diameters, while the ratio in the left lung was around 40%. However, as the ETT velocity increased from 0.5m/s to 2m/s, the particle delivery ratio in the right lung gradually decreased to around 45%, while the ratio in the left lung gradually increased to approximately 55%. This is due to a slight bias of the ETT direction towards the left lung. As the airflow of the ETT strengthened, the particle beam gradually deviated to the left lung, resulting in more particles being transported to the left lung. Since different particle delivery ratios lead to different regional deposition, which further affected the total deposition, this also explains the difference in the total DE in the lower respiratory tract in the three ETT cases.

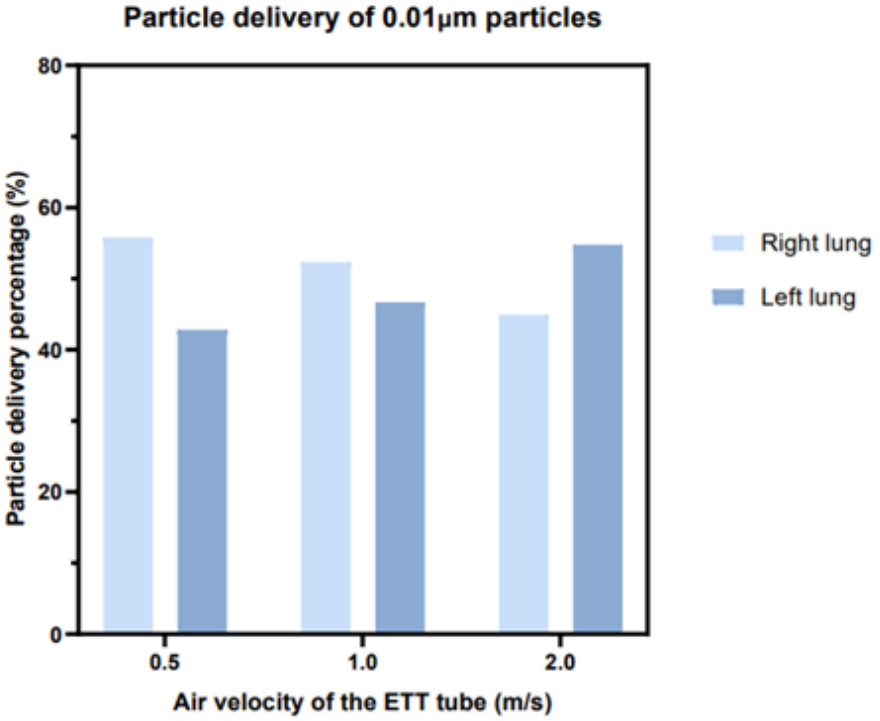
Particle delivery of 0.01μm particles
Particle delivery percentage (%)
80
60
40
20
0
0.5
1.0
2.0
Air velocity of the ETT tube (m/s)
Right lung
Left lung

(a)

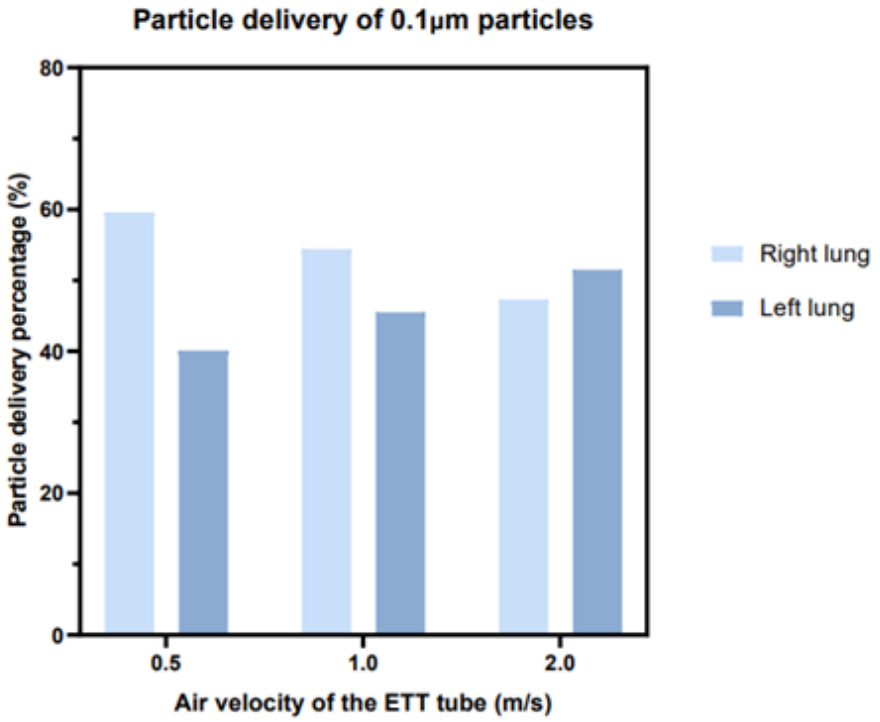
Particle delivery of 0.1μm particles
Particle delivery percentage (%)
80
60
40
20
0
0.5
1.0
2.0
Air velocity of the ETT tube (m/s)
Right lung
Left lung

(b)

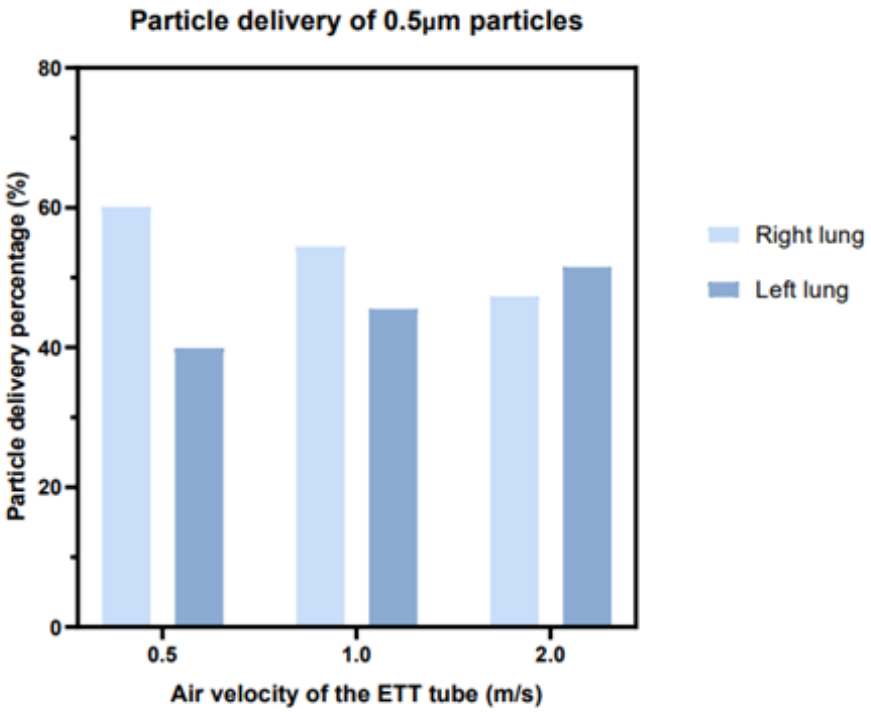
Particle delivery of 0.5μm particles
Particle delivery percentage (%)
80
60
40
20
0
0.5
1.0
2.0
Air velocity of the ETT tube (m/s)
Right lung
Left lung

(c)

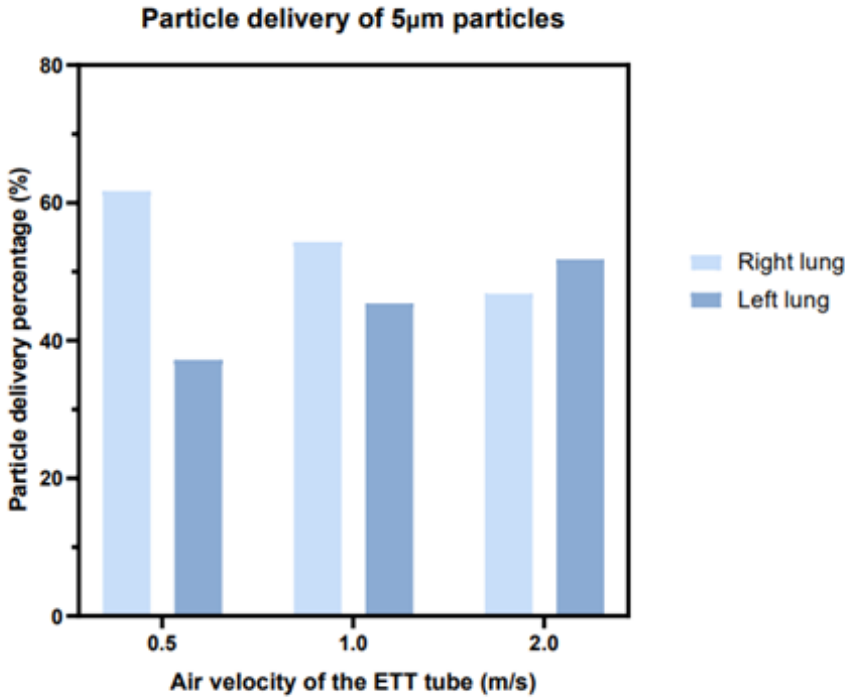
Particle delivery of 5μm particles
Particle delivery percentage (%)
80
60
40
20
0
0.5
1.0
2.0
Air velocity of the ETT tube (m/s)
Right lung
Left lung

(d)

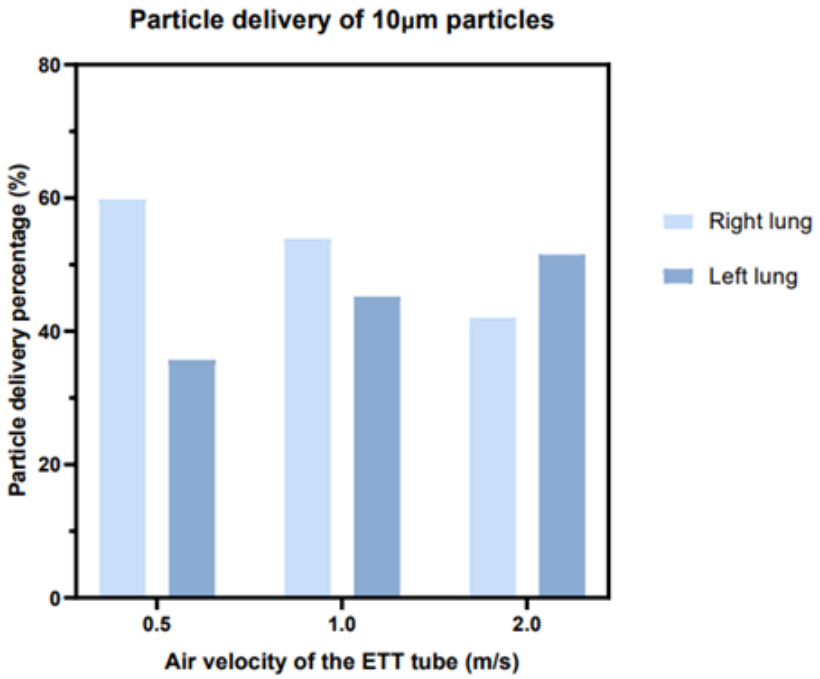

(e)

Fig.3.2.1.2 Particle delivery ratios in different lungs under different ETT jet flow (a)0.01μm (b)0.1μm (c)0.5μm (d)5μm (e)10μm

3.2.2 Deposition efficiency per generation in the tracheobronchial region

One of the advantages of the CFPD method is the ease of access to detailed regional deposition in the tracheobronchial model. DE for each generation of the ETT cases and autonomous respiratory case are shown in Fig.3.2.2.1 using Eq.13 and Eq.15. For the autonomous respiratory case, which is shown in Fig.3.2.2.1a, in the case of ultrafine particles, a focal point of 0.01μm was recorded in the 8th generation. The focal point is constant for ultrafine and fine particles approaching 2.5μm. For the ultrafine and fine particles, it is well adopted that a higher effective surface area leads to higher DE; as expected, in the CFPD model, the 8th generation possesses the highest total surface area, which has a higher probability of trapping particles (23). Meanwhile, the peak DE shifted to the 6th generation for the case of coarse particles

(5 and 10μm), especially reaching the value of around 18% at 10μm. Theoretically, coarse particles tend to concentrate in the region of high-velocity fluid flow because of their high inertia and relaxation time properties. In this sense, the most deposited particles were recorded in the 6th generation, where fluid acceleration occurred(23).

The same deposition mechanism can also be applied to ETT cases. For ultrafine and fine particles, the three ETT cases exhibited the same focal points and trends in terms of local DE. In the 0.5 m/s case, the focal points are observed at the 5th and 8th generations. In the 1 m/s case, the focal point is at the 7th generation. In the 2 m/s case, the focal point is at the 6th generation. As described in Chapter.3.2.1, the different ETT flow velocities result in variations in particle delivery to different lung lobes, which means the particles cannot be delivered evenly to each lung lobe by airflow as in the autonomous respiratory case. Therefore, it led to differences in the effective total surface area for each case. The 0.5 m/s case possesses the highest effective total surface area at the 5th and 8th generations, while the 1 m/s case exhibits it at the 7th generation, and the 2 m/s case exhibits it at the 6th generation. For coarse particles, the peak DEs in the three cases are observed at the 7th generation (0.5m/s), around the 5th and 6th generations (1m/s), and at the 6th generation (2m/s), respectively, which is consistent with the airflow field analysis described in 3.1. In the 0.5 m/s case, the velocity acceleration was mainly concentrated at the 6th and 7th generations. In the 1 m/s and 2 m/s cases, the velocity accelerations were primarily distributed between the 5th and 6th generations. The specific velocity characteristics of the three cases contribute to the regional DE characteristics.

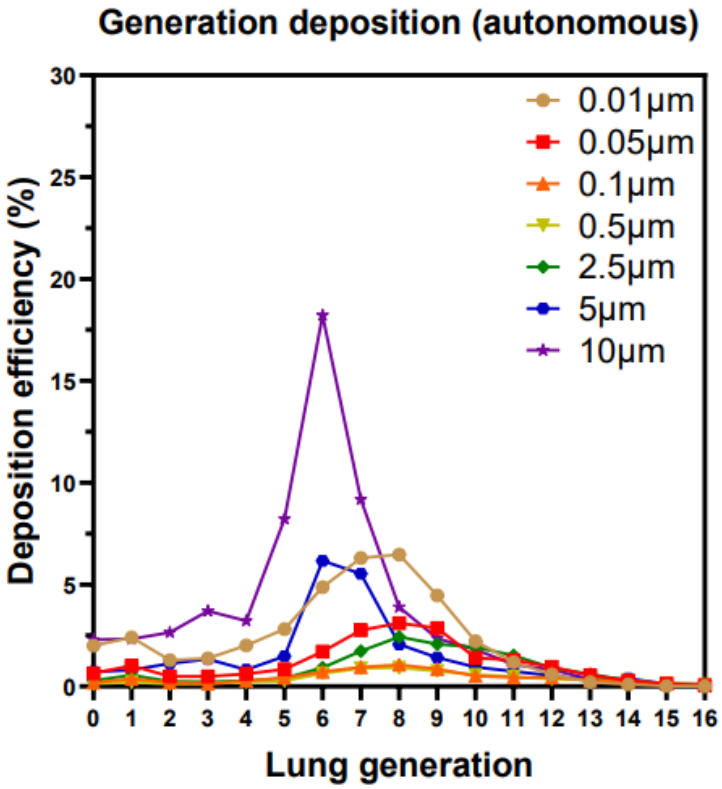
Generation deposition (autonomous)
Deposition efficiency (%)
Lung generation
0.01μm
0.05μm
0.1μm
0.5μm
2.5μm
5μm
10μm
0 5 10 15 20 25 30
0 1 2 3 4 5 6 7 8 9 10 11 12 13 14 15 16

(a)

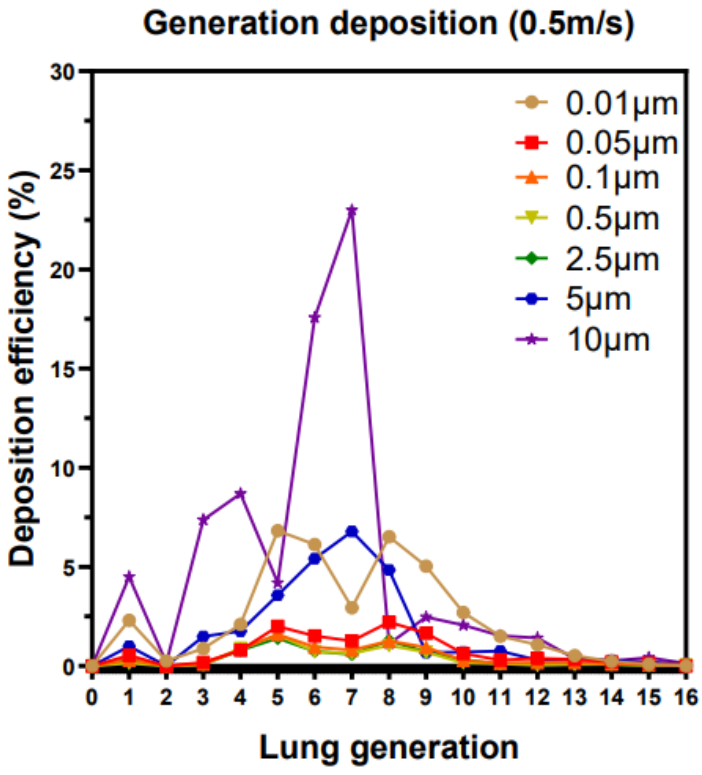
Generation deposition (0.5m/s)
Deposition efficiency (%)
Lung generation
0.01μm
0.05μm
0.1μm
0.5μm
2.5μm
5μm
10μm
0 5 10 15 20 25 30
0 1 2 3 4 5 6 7 8 9 10 11 12 13 14 15 16

(b)

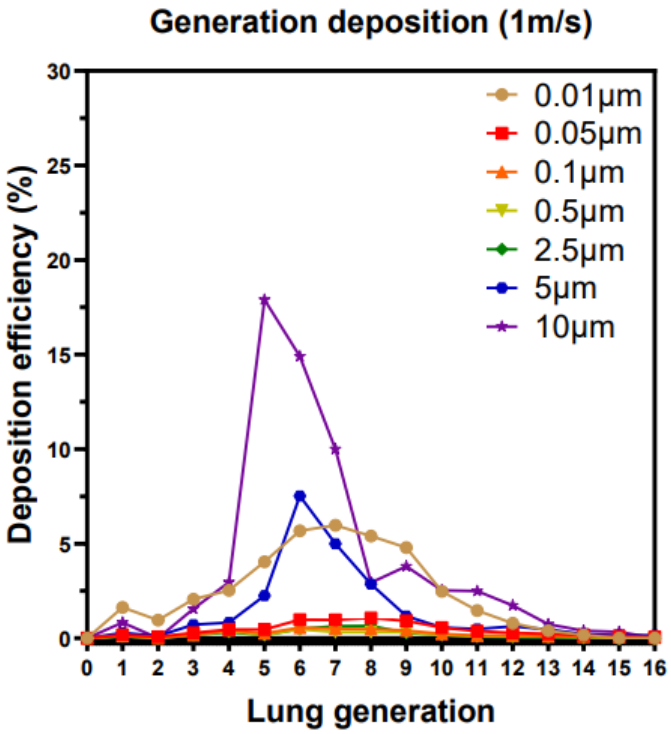

(c)

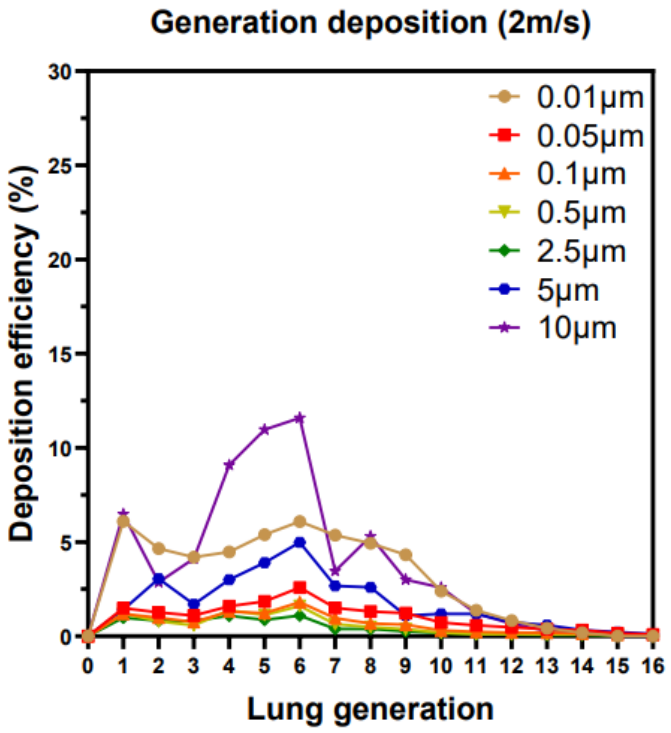

(d)

Fig.3.2.2.1 Deposition fraction per generation of selected particle sizes in ETT and autonomous respiratory cases

In addition, compared to the autonomous respiratory case, the three ETT cases exhibit different characteristics in the 1st and 2nd generations. Particles of various sizes show certain DE in the 1st generation, but the DE significantly decreases at the 2nd generation. Specifically, in the 0.5 m/s and 1 m/s cases, most sizes of particles have minimal depositions at the 2nd generation. This phenomenon can be explained by Fig.3.2.2.2 and Fig.3.2.2.3.

Fig.3.2.2.2 shows the particle tracking and deposition conditions in 1st and 2nd generations with a particle size of 0.01μm. The particle tracking images indicate that particles were injected from the ETT and collided with the 1st generation wall in the bifurcation area without being fully mixed with the flow in the trachea, before which the particles were separately delivered into the right and left lungs. It is noticeable that even in the 2nd generation, particles were not well mixed with air, just close to the lower area of the airway, rather than evenly distributed in the domain. The deposition of particles at the 1st generation occurs due to collisions between particles and the bifurcation region of the 1st generation wall, which increases the likelihood of DE. However, the difference among the three cases lies in the fact that with an increase in ETT jet flow, the collisions between particles and the bifurcation region of the 1st generation become stronger. These intense collisions enhanced the mixing of particles with the overall airflow, resulting in a more uniform distribution of particles within the airway. Consequently, particles have a higher probability of deposition. This also explains why the DE increased at the 2nd generation as the ETT jet increased. Fig.3.2.2.3 shows the particle tracking and deposition conditions in 1st and 2nd generations with a particle size of 10μm. Similar to 0.01μm particles, the collision between the jet and the bifurcation region of the 1st generation leads to particle deposition at the bifurcation. However, due to the poor diffusion characteristics of coarse particles, after the collision between the jet and the bifurcation region, coarse particles still have limited mixing with the airflow compared to ultrafine and fine particles. As a result, despite the relatively high velocity at the 2nd generation in the three cases, few particles were deposited in the 2nd generation.

In conclusion, compared to autonomous respiratory cases, the use of the ETT results in different regional deposition characteristics for ultrafine, fine, and coarse particles. Furthermore, these deposition characteristics vary depending on the ETT jet flow rate.

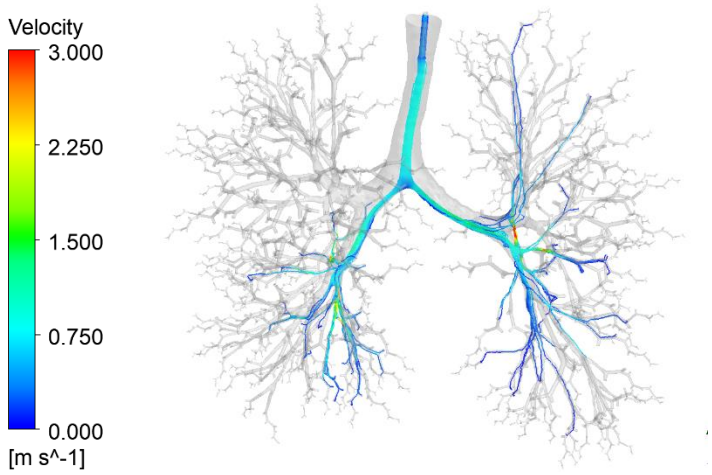

(a)

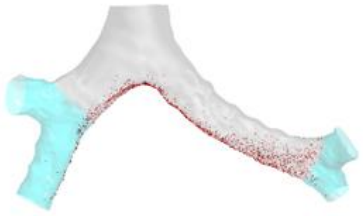

(d)

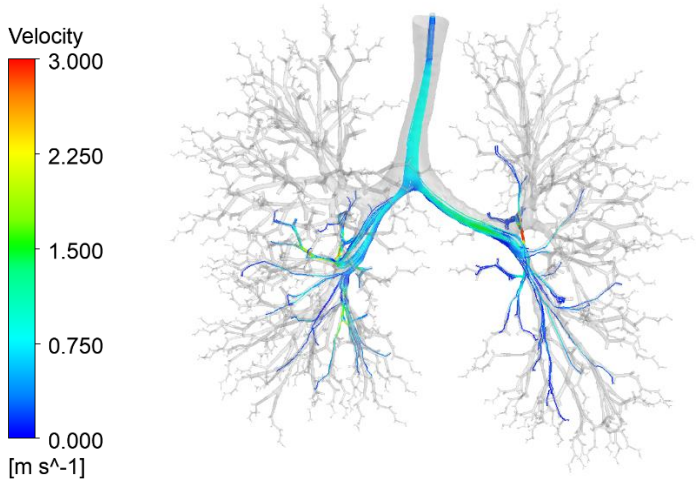

(b)

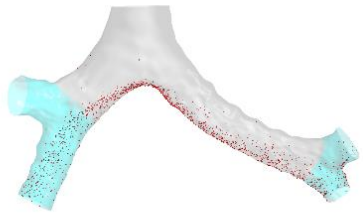

(e)

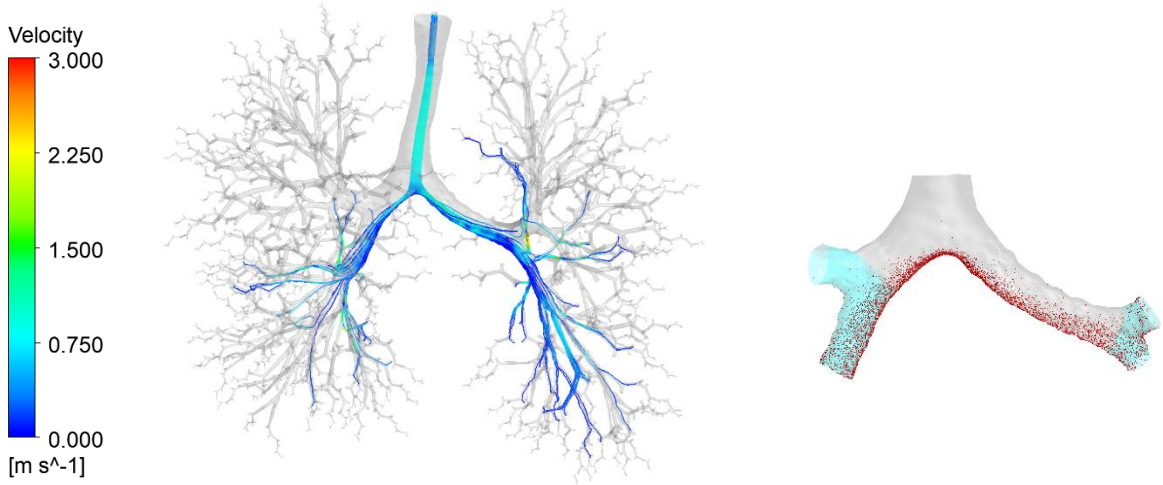

(c) (f)

Fig.3.2.2.2 Particle tracking and deposition conditions with particle size of 0.01µm in ETT cases (a) Particle tracking in the case of 0.5m/s (b) Particle tracking in the case of 1m/s (c) Particle tracking in the case of 2m/s (d) Deposition condition in 1st and 2nd generations in the case of 0.5m/s (e) Deposition condition in 1st and 2nd generations in the case of 1m/s (f)Deposition condition in 1st and 2nd generations in the case of 2m/s

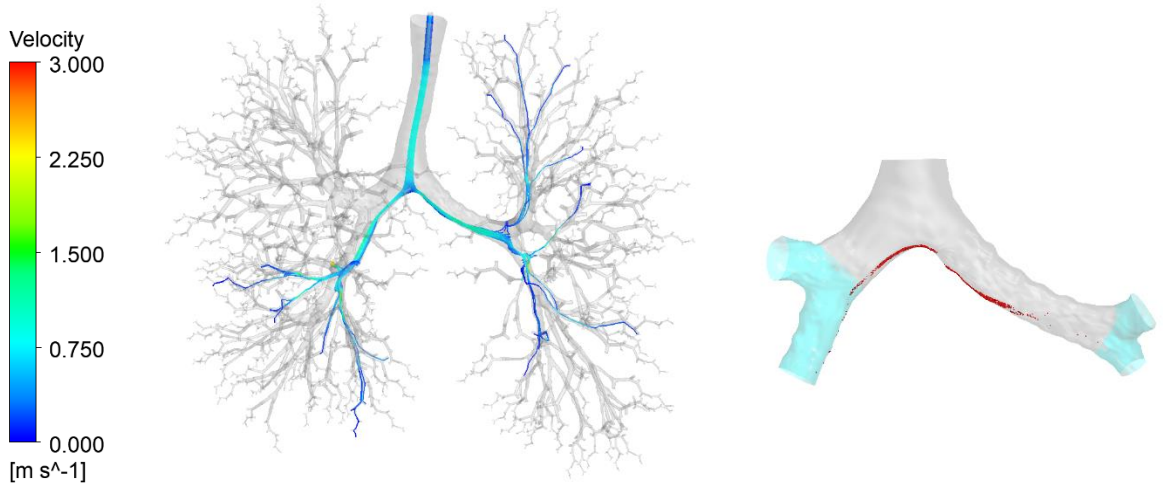

(a) (d)

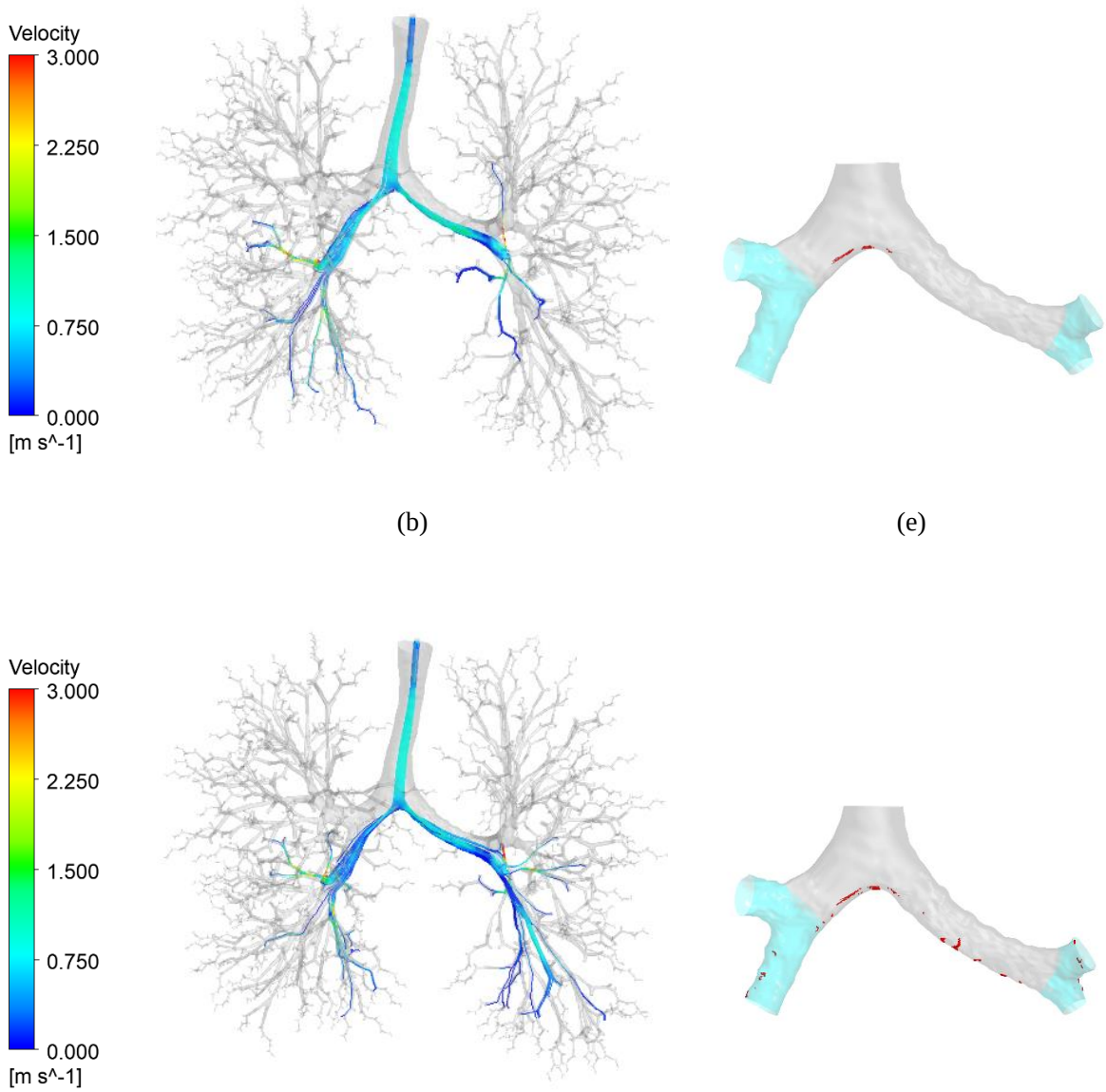

Fig.3.2.2.3 Particle tracking and deposition conditions with particle size of 10μm in ETT cases (a) Particle tracking in the case of 0.5m/s (b) Particle tracking in the case of 1m/s (c) Particle tracking in the case of 2m/s (d) Deposition condition in 1st and 2nd generations in the case of 0.5m/s (e) Deposition condition in 1st and 2nd generations in the case of 1m/s (f)Deposition condition in 1st and 2nd generations in the case of 2m/s

3.2.3 Deposition efficiency in different lobes

Lobar deposition can numerically evaluate the effect of ETT jet flow rate on the particle deposition characteristic. Fig.3.2.3.1 shows the human lung regionalization including five lobes: RUL (right upper lung), RML (right middle lung), RLL (right lower lung), LUL (left upper lung), and LLL (left lower lung). The lobe deposition in the thoracic region in the ETT casesis shown in Fig.3.2.3.2 and was calculated using Eq.13. From the Fig.3.2.3.2, it can be observed that for all selected particle sizes, the DE in RUL is zero, and in most cases, the DE in LUL is also close to or equal to zero. This is because the ETT jet flow caused particle beams to collide with the bifurcation region of the 1st generation, resulting in particle flow mainly flowing towards RLL and LLL along the lower wall of the 1st generation. Although there is a certain ventilation rate in RUL and LUL, particle delivery by ETT resulted in very few particles entering RLL and LLL. Regarding the DE in RLL and LLL, it decreases initially and then increases with increasing particle diameter, which is consistent with the general DE in the human lower airway shown in Figure 3.2.1.1.

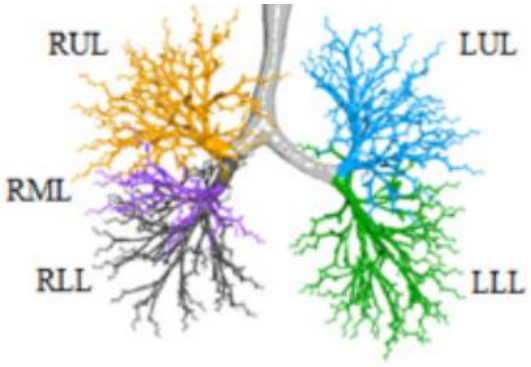

Fig.3.2.3.1 Human lung regionalization

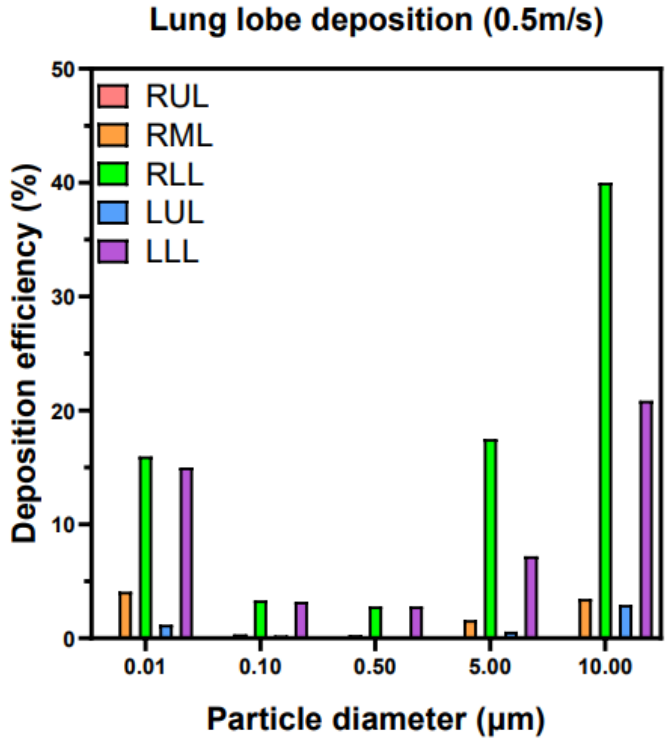
Lung lobe deposition (0.5m/s)
RUL
RML
RLL
LUL
LLL
Deposition efficiency (%)
0
10
20
30
40
50
0.01
0.10
0.50
5.00
10.00
Particle diameter (μm)

(a)

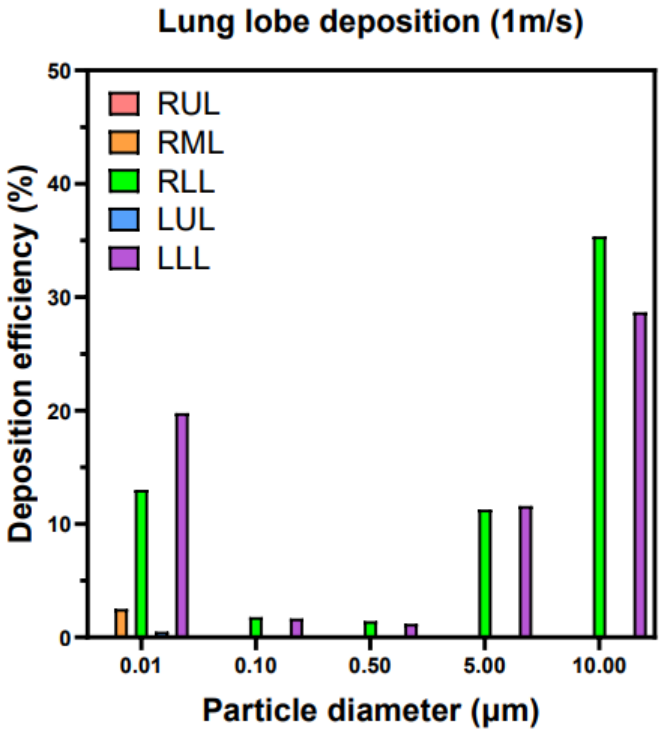
Lung lobe deposition (1m/s)
RUL
RML
RLL
LUL
LLL
Deposition efficiency (%)
0
10
20
30
40
50
0.01
0.10
0.50
5.00
10.00
Particle diameter (μm)

(b)

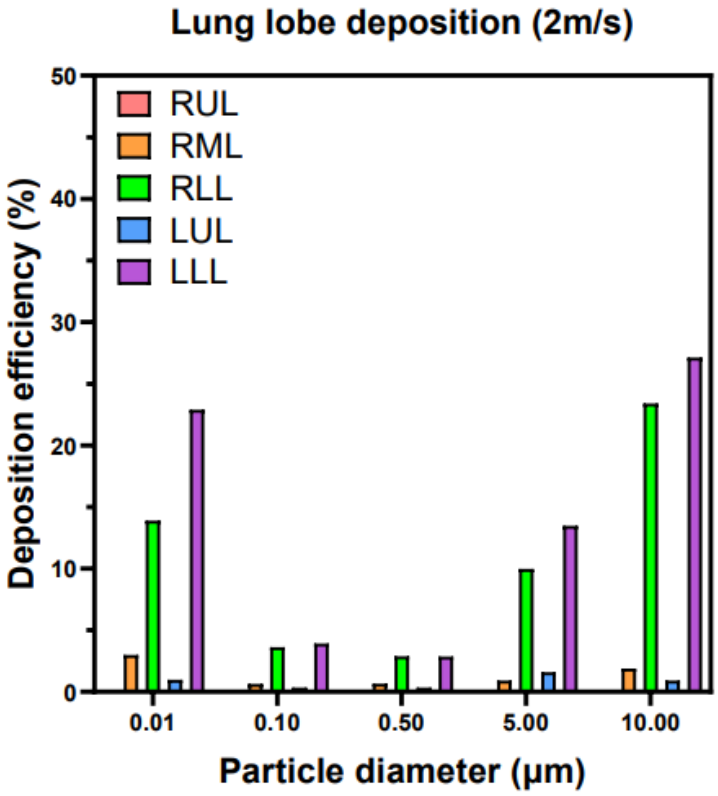

(c)

Fig.3.2.3.2 Lung lobe deposition with ETT velocity of (a) 0.5m/s, (b) 1m/s, (c) 2m/s for the selected particle size

Furthermore, as the ETT jet flow rate increased for particles of the same size (0.01μm, 5μm, 10μm), the DE in the right lung gradually decreased while the DE in the left lung gradually increased. Specifically, in the 0.5 m/s case, the DE in the right lung was higher than that in the left lung, but in the 2 m/s case, it was reversed. As shown in Figure 3.2.1.2, with increasing ETT jet flow rate, particle delivery in the left lung increased while particle delivery in the right lung decreased, and particle delivery directly affected DE. Fig.3.2.3.3 shows the visual images of particle deposition distribution in the human lower airway in the ETT cases with particle sizes of 0.01μm and 10μm. As observed, although 10μm particles exhibit higher DE in the lower respiratory tract compared to 0.01μm particles, the distribution of 0.01μm particles is more uniform, as evident from the graph. The 10μm particles tend to predominantly settle at specific

locations, whereas the 0.01μm particles uniformly deposit across various regions of the lower respiratory tract. This discrepancy is attributed to the sedimentation mechanisms of ultrafine and 10μm particles. Ultrafine particles primarily undergo diffusion settling, while 10μm particles are influenced by inertial settling.

Thus, it can be observed that in the context of drug delivery using an ETT, the main deposition sites for drugs are the RLL and LLL, while DE in other areas is limited. Moreover, by adjusting the ETT jet flow rate, the DE in different lung lobes can be altered to some extent, with more pronounced effects on ultrafine and coarse particles.

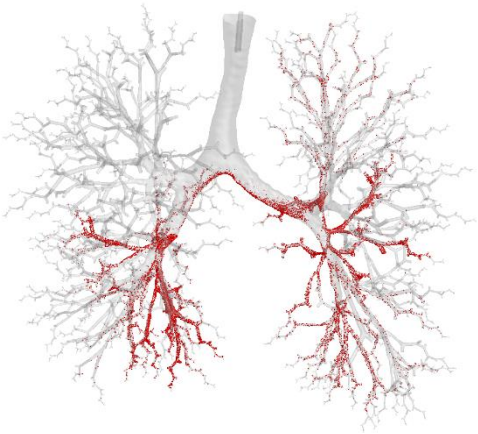

(a)

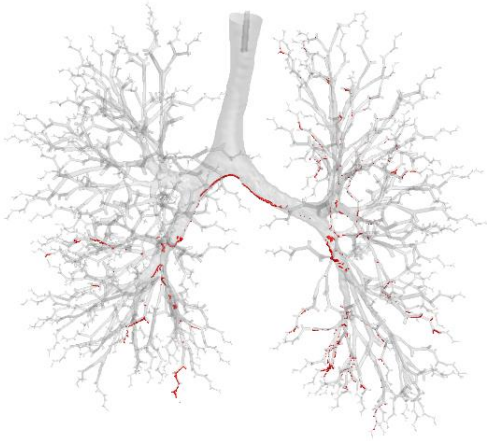

(b)

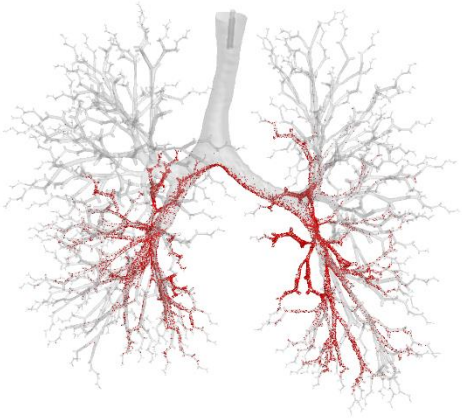

(c)

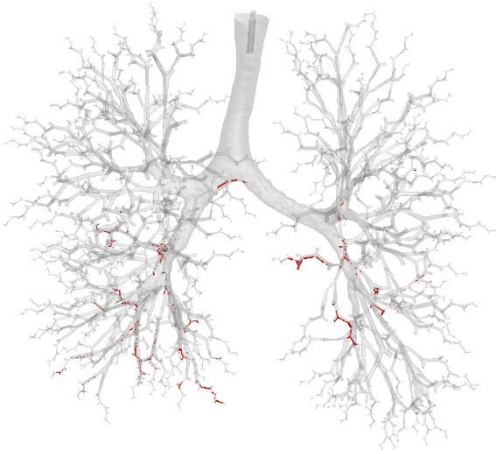

(d)

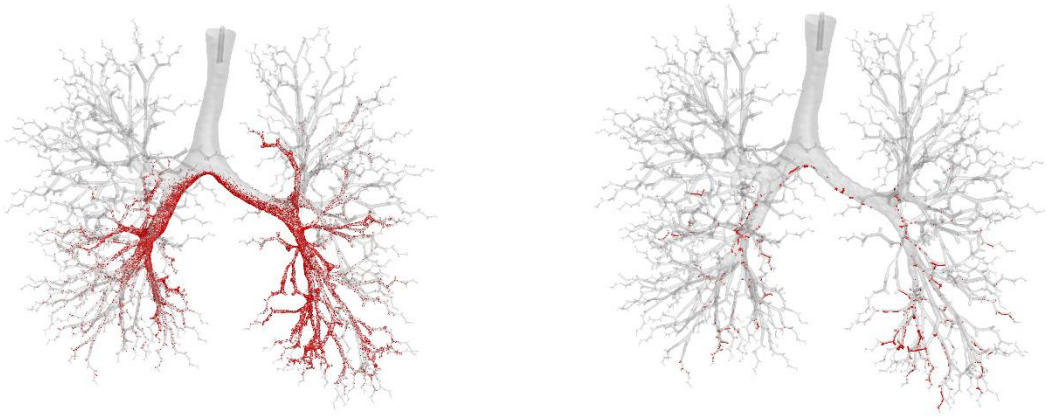

(e) (f)

Fig.3.2.3.3 Visual images of particle deposition distribution in human lower airway (a) Deposition distribution with particle size of 0.01μm in 0.5m/s case (b) Deposition distribution with particle size of 10μm in 0.5m/s case (c) Deposition distribution with particle size of 0.01μm in 1m/s case (d) Deposition distribution with particle size of 10μm in 1m/s case (e) Deposition distribution with particle size of 0.01μm in 2m/s case (f) Deposition distribution with particle size of 10μm in 2 m/s case

3.2.4 Penetration efficiency of particles into the 17th generation

The comparison of PE between cases with an ETT and the autonomous respiratory case, considering different selected particle sizes, is presented in Fig.3.2.4.1. The data in this figure provides valuable insights into the percentage of particles that successfully reach the 17^{th} generation of the airway. The PE values were meticulously calculated using Eq.16, ensuring accurate and reliable results. Upon a comprehensive analysis of the deposition characteristics of the human lower airway (as displayed in Fig. 3.2.1.1), a distinct trend emerges. As particle size increases in all four cases, PE exhibits an initial gradual increase, followed by a subsequent gradual decrease. This behavior is attributed to the interplay between particle size, airway dynamics, and deposition mechanisms.

However, the presence of the ETT introduces a significant differentiation in the outcomes. The ETT cases demonstrate an impressive ability to prevent particle deposition in the human upper airway, resulting

in notably higher PE values compared to the autonomous respiratory case. This effect is particularly prominent for particles with sizes of 0.01μm and 10μm, where the ETT's contribution to enhancing particle delivery to the lower regions of the airway is most pronounced. The implications of these findings hold particular importance for chemotherapy treatments. The application of an ETT tube can serve as a powerful tool in maximizing the delivery of therapeutic particles to the deeper regions of the respiratory system. By precisely targeting the 17th generation of the airway and even reaching the alveoli, the ETT enables an optimized drug delivery strategy. This heightened precision in drug delivery holds the potential to increase the efficacy of chemotherapy, leading to improved therapeutic success and, ultimately, better treatment outcomes for patients.

The significance of these research outcomes extends beyond chemotherapy. The improved understanding of ventilation efficiency in the lower airway, facilitated by the use of an ETT, offers valuable guidance for the development of advanced static ventilators. This knowledge empowers researchers and medical practitioners to design and implement more effective respiratory support systems, enhancing patient care and critical care interventions.

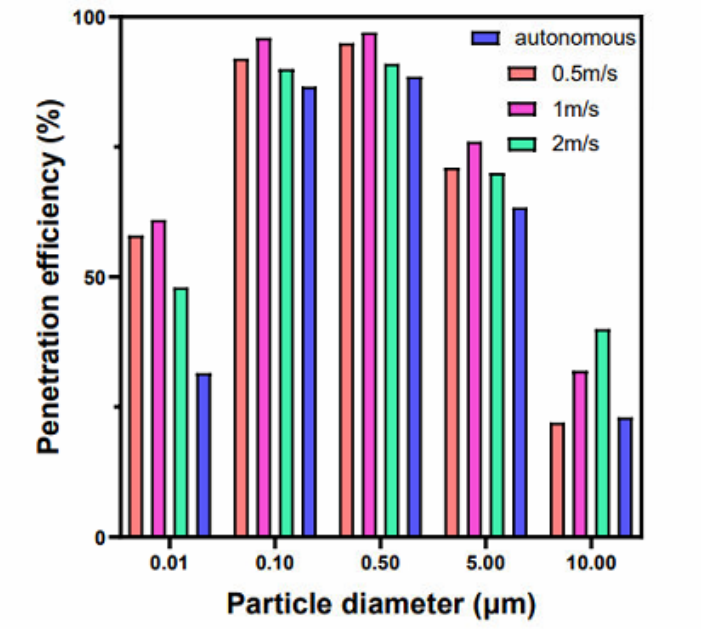

Fig.3.2.4.1 Penetration efficiency of particles into the 17th generation for ETT cases and autonomous respiratory case for the selected particle sizes

3.3 Ventilation efficiency analysis of the static ventilator

The airflow characteristics of Cases 1-5 are depicted in Fig.3.3.1, which shows the velocity magnitude in the ETT, trachea, and the 1st generation. At a given inlet flow rate of 1 L/min, in the first three cases (1-3), the peak velocity was observed in the inner tube of the ETT. However, for Cases 1 and 2, the jet stream was defined as the supplied air; hence, the airflow exited the inner tube and deeply hit the airway wall before entering the 1st generation (marked by the red frame). In contrast, in Case 3, the jet stream was assumed to be a suction flow, which caused the flow to vanish in the trachea region. For the higher flow rate of 10 L/min (Cases 4 and 5), the flow distribution characteristics are observed to be almost homogeneous with Cases 2 and 3, respectively, which show independence of airflow distribution with the increment in flow rates.

The difference between Cases 1 and 2 can be clarified using the streamlined distribution, as shown in Fig. 3.3.2. Specifically, fluid flow could deeply penetrate the bronchial region because of the lack of suction function of the ETT. Meanwhile, the assumption of suction flow using the outer tube of the ETT partially hinders the delivery of fluid flows deeper into the bronchial airways. In Case 3, the airstream supplied by the outer tube of the ETT was almost exhausted via the inner tube. In Case 4, the streamlined distribution delivered a consistent phenomenon with Case 2; however, when comparing the characteristics of Cases 3 and 5, the streamlined distribution suggested that under the effects of higher flow rates, the fluid flow could be transferred to the entrance of the first bifurcation.

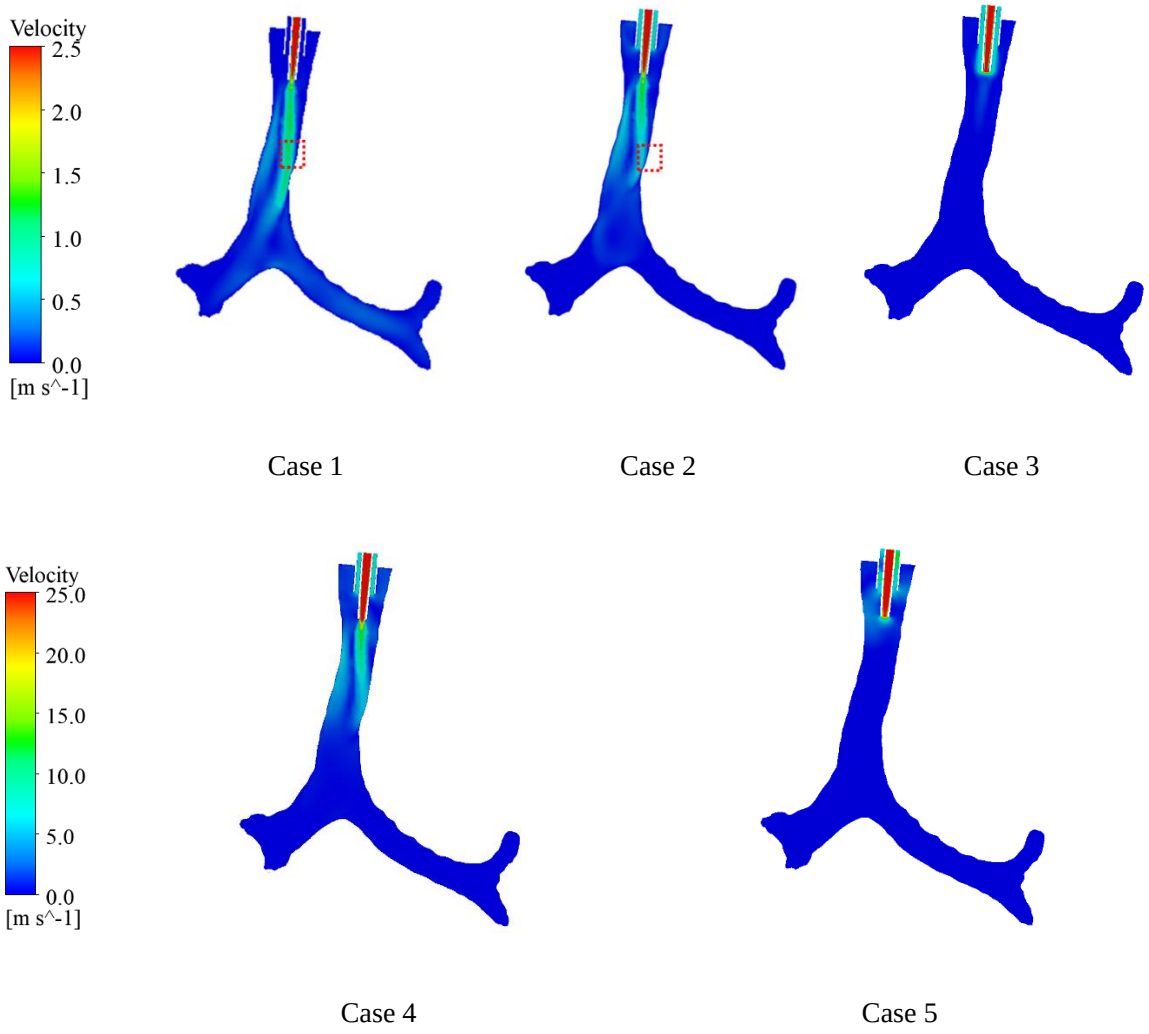

Fig.3.3.1 Airflow characteristics in the trachea area under different configurations and flow rates

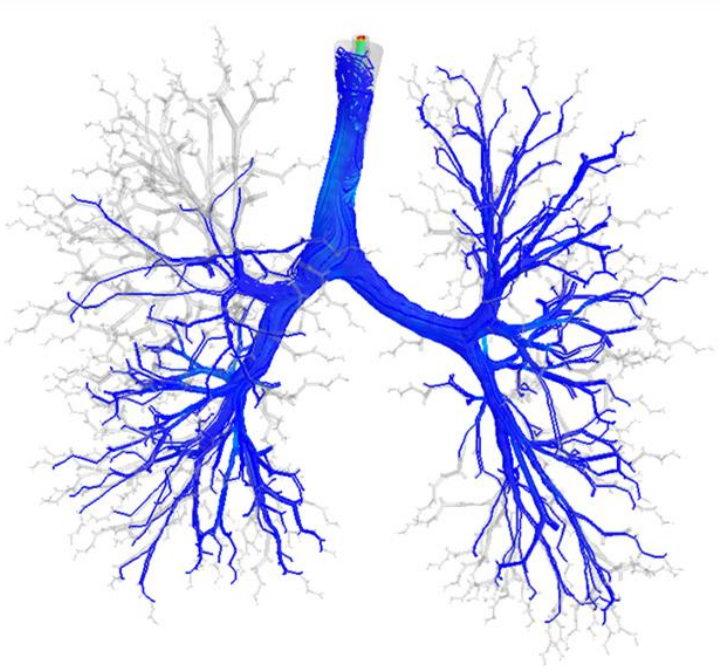

Case 1

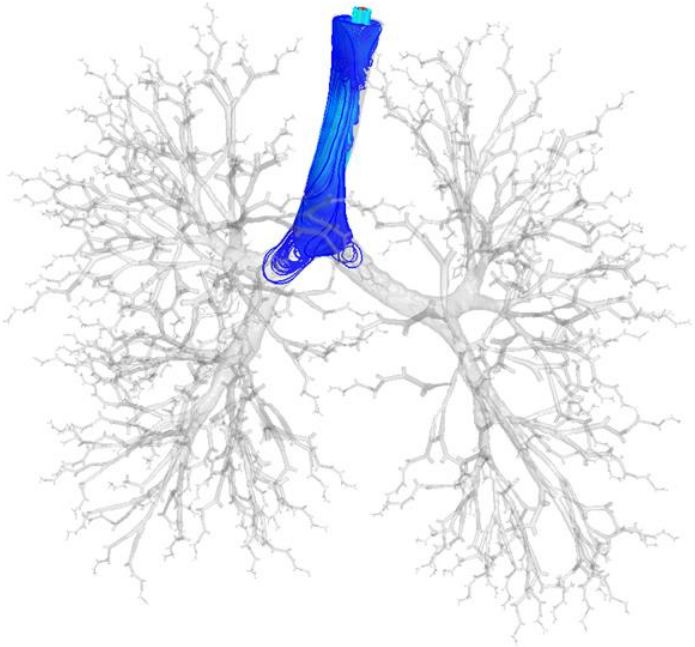

Case 2

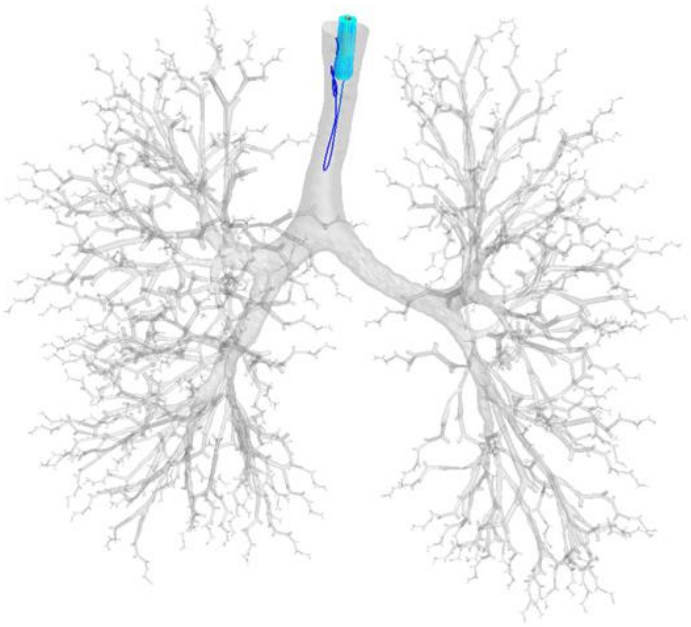

Case 3

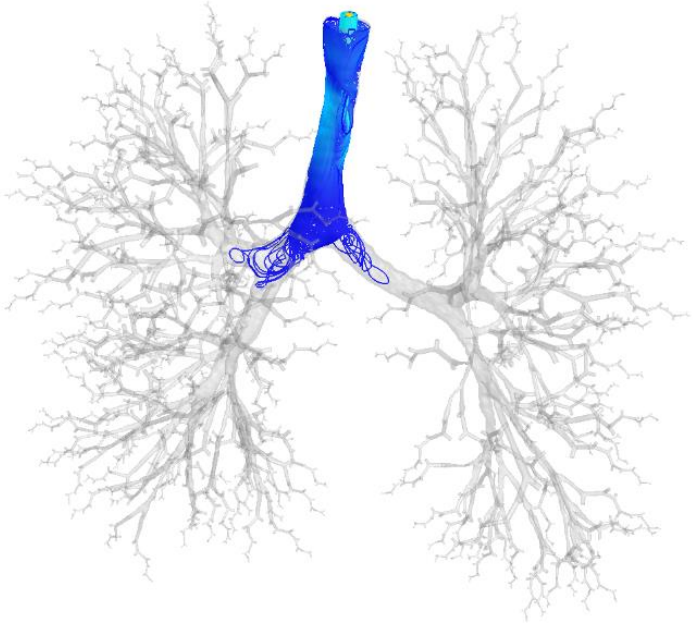

Case 4

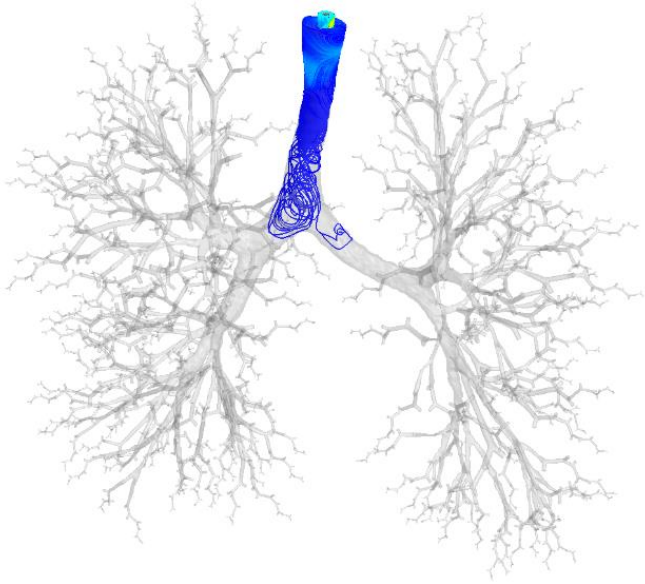

Case 5

Fig.3.3.2. Streamline distributions in the static ventilator model under different configurations and flow rates

Theoretically, the value of SVE3 indicates dimensionless time scale for fresh air delivery and the airflow arrival time from the inlet to a certain point; hence, it can be regarded as a significant parameter for judging ventilation efficiency. Thus, a higher SVE3 value is associated with a lower ventilation efficiency and vice versa. In these cases, SVE3 values are normalized by the nominal time constant defined as V/Q. SVE 3 contours of Cases 1-5 are displayed in Fig.3.3.3. For Case 1, the result indicates that the SVE3 value gradually increased along with the generation order from the inlet to the 16th generation, except for the surrounding area of the ETT, as the jet-stream pushed the air quickly to the trachea and bronchial region, as discussed in the previous section. As expected, high SVE3 was observed in this region. The maximum value appeared at the top left-end position with a value of 4.72, which suggested a relatively good ventilation efficiency in the autonomous respiratory condition with the application of ETT. However, in Cases 2 to 5, the values were much higher than those in Case 1 in the bronchioles. Therefore, for Cases 2 to 5, the trachea-area characteristics were analyzed and displayed. Specifically, good ventilation can be

achieved in the tracheal region, while the value of SVE3 suddenly increases to approximately 2 in the 1st bifurcation of Case 2. For Case 3, a high SVE3 was observed in the entire trachea and the 1st bifurcation, which is the consequence of the intermediate exhaust of the fluid flow through the inner tube. Under the effects of increasing flow rate, the distribution and magnitude of SVE3 in Case 4 were almost consistent with Case 2; meanwhile, the vicinity around the ETT portrayed a relatively low SVE3 (approximately 0.5) in Case 5. The age of air contour of the five cases is shown in Fig.3.3.4, which showed similar characteristics to SVE 3. Case 1 showed a low value of the age of air. For the boundary conditions of Cases 2 and 3, the values separately got lower as the flow rate increased.

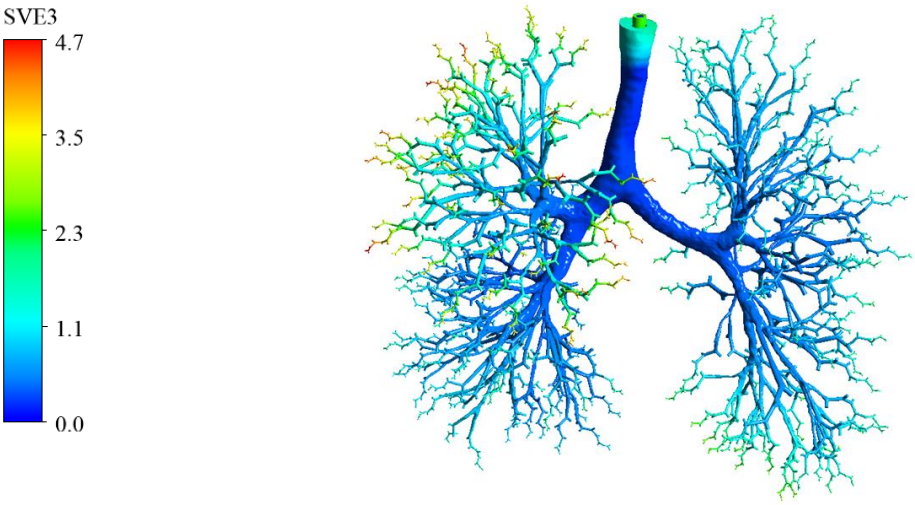

Case 1

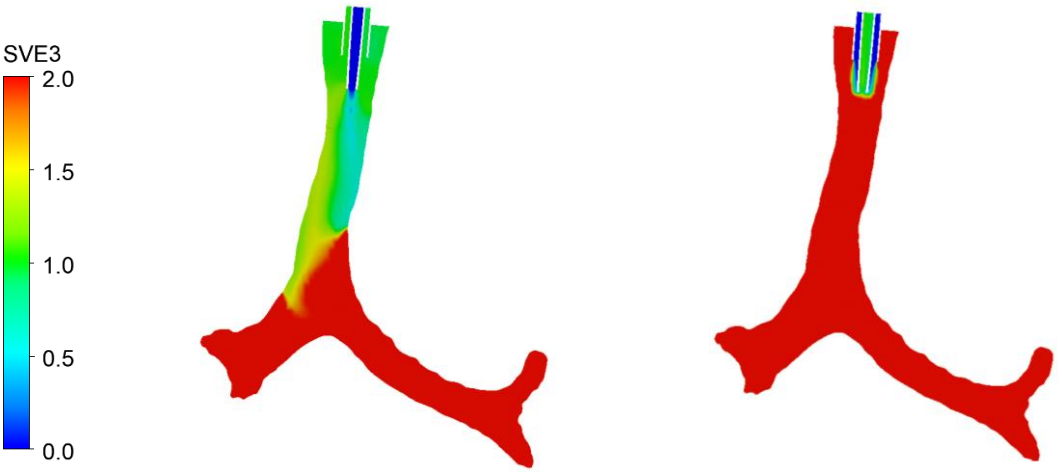

Case 2 Case 3

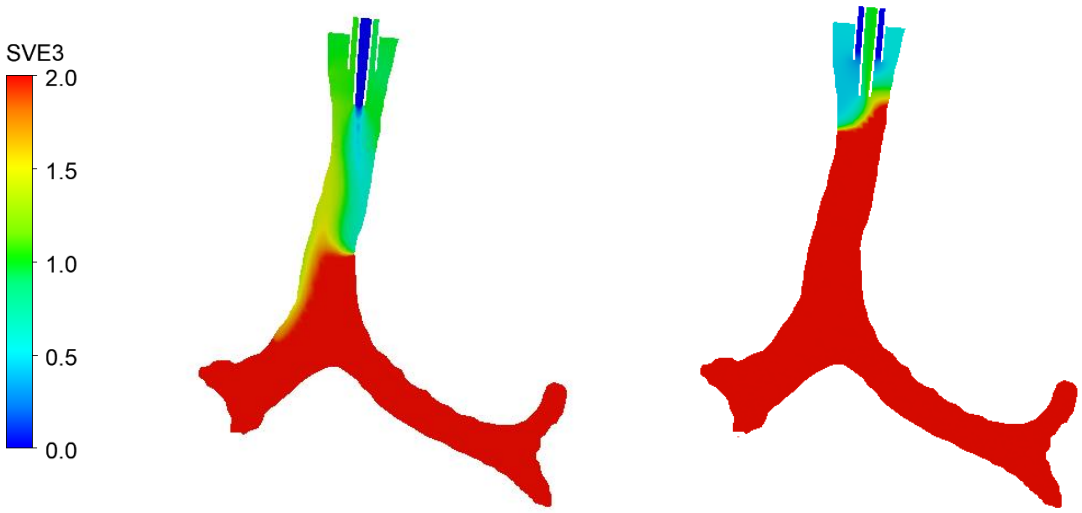

Case 4 Case 5

Fig.3.3.3. SVE 3 characteristics in the ETT-tracheobronchial model of Case 1 and the trachea area of Cases 2 to 5

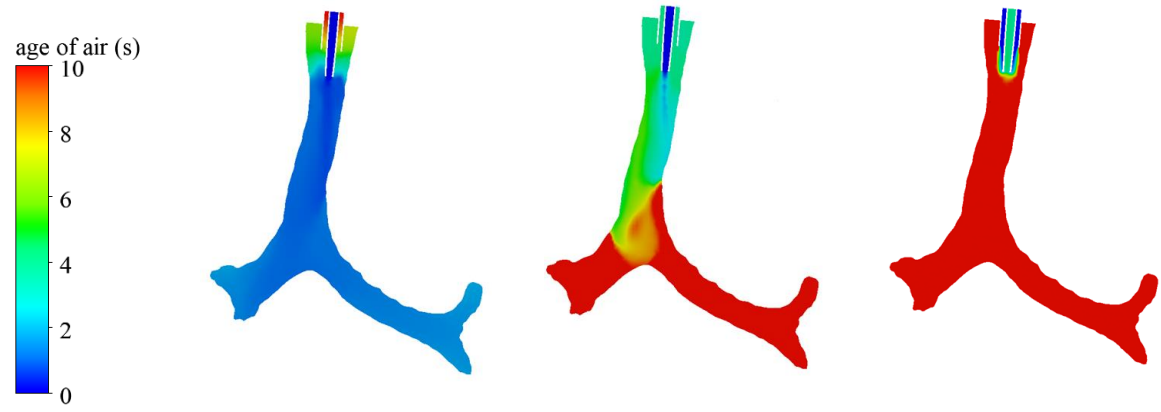

Case 1 Case 2 Case 3

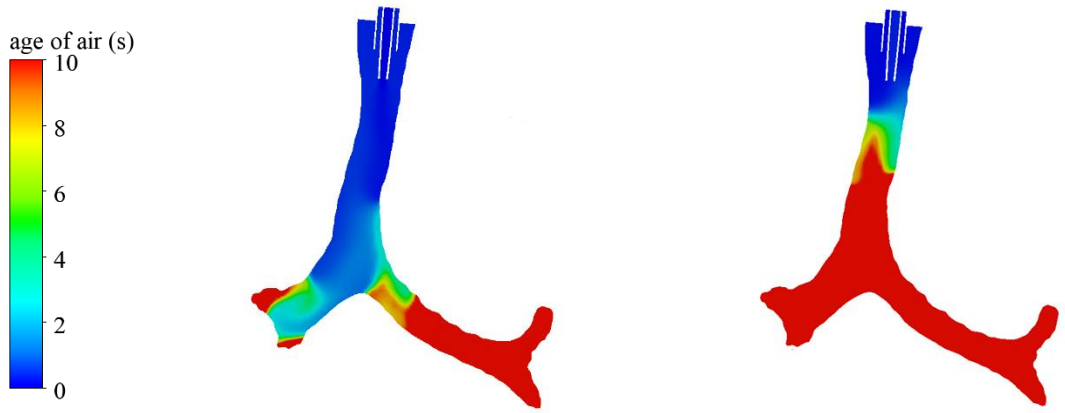

Fig.3.3.4. Age of air characteristics in the upper region under different configurations and flow rates

From the results, the alternation in the operation configurations could profoundly impact the delivery of fresh air to the trachea and bronchioles. Using the inner tube as the air-supplying conduit would benefit from conveying air to deeper regions. The increment of supply flow rates exerted certain impact on the ventilation efficiency in the lower airway, as shown in Fig.3.3.4. Concerning ventilation efficiency, only Case 1 showed good ventilation efficiency throughout the model. By applying the artificial ventilation configurations, the appearance of the air-jet stream from the ETT could only offer good ventilation in the trachea region. The meager ventilation rates in Cases 3 and 5 revealed that the realistic configuration currently used in the MV might not be appropriate compared to our study's assumptions (Cases 2 and 4).

4. Conclusion

This study successfully investigated the delivery of drug particles in the human lower respiratory tract by using ETT. The results can provide valuable insights for the chemotherapy of pulmonary tumors. Additionally, this study proposed a novel static ventilator design that minimizes lung injury, particularly for severe patients who cannot conduct autonomous respiratory.

In the context of ETT drug delivery for pulmonary tumors treatment, the following three conclusions can be drawn: (1) ETT injection chemotherapy and inhalation chemotherapy exhibit different regional deposition characteristics, and the intensity of the ETT jet flow significantly affects the deposition characteristics. (2) ETT jet flow leads to particle deposition mainly in LLL and RLL, and different ETT jet flow intensities influence the particle delivery proportion and DE in lung lobes. As the ETT jet flow intensity increases, the particle delivery proportion in the left lung gradually increases while it decreases in the right lung, resulting in changes in the DE in different lobes, especially in LLL and RLL. (3) Compared to inhalation chemotherapy, ETT injection chemotherapy can significantly enhance PE in the 17^{th} generation, which facilitates drug delivery to deeper regions and alveoli in the lower respiratory tract.

For the static ventilator development, two main conclusions can be drawn: (1) Compared to the outer tube, importing air through the inner tube provides better ventilation efficiency in the lower respiratory tract. (2) Airflow rate contributes to ventilation efficiency while increasing airflow rate enhances ventilation efficiency in the lower respiratory tract.

In conclusion, this study utilized an ETT to analyze particle deposition characteristics in the human lower airway. The findings offer valuable insights that can be used as a reference for tumor treatment, specifically in terms of chemotherapy. Additionally, the analysis of ventilation efficiency in the lower airway provides valuable guidance for the development of static ventilators. By bridging this research gap, our study contributes to the understanding of respiratory dynamics and provides crucial information for both medical treatments and the advancement of ventilator technology. These results hold significant potential to enhance patient care and respiratory therapies, ultimately benefiting individuals' health and well-being.

5. Reference

1. Siegel R, Ma J, Zou Z, Jemal A. Cancer statistics, 2014. CA Cancer J Clin [Internet]. 2014 Jan 7 [cited 2023 Apr 28];64(1):9–29. Available from: https://europepmc.org/article/med/24399786
2. Park CM, Goo JM, Lee HJ, Kim MA, Lee CH, Kang MJ. Tumors in the Tracheobronchial Tree: CT and FDG PET Features1. https://doi.org/101148/rg291085126 [Internet]. 2009 Jan 1 [cited 2023 Jun 9];29(1):55–71. Available from: https://pubs.rsna.org/doi/10.1148/rg.291085126
3. Macchiarini P. Primary tracheal tumours. Lancet Oncol. 2006 Jan 1;7(1):83–91.
4. Marino P, Pampallona S, Preatoni A, Cantoni A, Invernizzi F. Chemotherapy vs Supportive Care in Advanced Non-Small-Cell Lung Cancer: Results of a Meta-analysis of the Literature. Chest. 1994 Sep 1;106(3):861–5.
5. New chemotherapeutic agents prolong survival and improve quality of life in non-small cell lung cancer: a review of the literature and future directions. | Clinical Cancer Research | American Association for Cancer Research [Internet]. [cited 2023 Jun 9]. Available from: https://aacrjournals.org/clincancerres/article/4/5/1087/7510/New-chemotherapeutic-agents-prolong-survival-and
6. Tatsumura T, Koyama S, Tsujimoto M, Kitagawa M, Kagamimori S. Further study of nebulisation chemotherapy, a new chemotherapeutic method in the treatment of lung carcinomas: fundamental and clinical. Br J Cancer 1993 686 [Internet]. 1993 [cited 2023 Apr 28];68(6):1146–9. Available from: https://www.nature.com/articles/bjc1993495
7. Tatsumura T, Yamamoto K, Murakami A, Tsuda M, Sugiyama S. [New chemotherapeutic method for the treatment of tracheal and bronchial cancers--nebulization chemotherapy]. Gan No Rinsho [Internet]. 1983 Jun 1 [cited 2023 Apr 28];29(7):765–70. Available from: https://europepmc.org/article/med/6308308
8. Otterson GA, Villalona-Calero MA, Sharma S, Kris MG, Imondi A, Gerber M, et al. Phase I Study of Inhaled Doxorubicin for Patients with Metastatic Tumors to the Lungs. Clin Cancer Res [Internet]. 2007

Feb 15 [cited 2023 Jun 9];13(4):1246–52. Available from: https://dx.doi.org/10.1158/1078-0432.CCR-06-1096

9. Huland E, Heinzer H, Huland H. Inhaled interleukin-2 in combination with low-dose systemic interleukin-2 and interferon α in patients with pulmonary metastatic renal-cell carcinoma: effectiveness and toxicity of mainly local treatment. J Cancer Res Clin Oncol [Internet]. 1994 Feb [cited 2023 Jun 9];120(4):221–8. Available from: https://link.springer.com/article/10.1007/BF01372560

10. Taratula O, Garbuzenko OB, Chen AM, Minko T. Innovative strategy for treatment of lung cancer: targeted nanotechnology-based inhalation co-delivery of anticancer drugs and siRNA. http://dx.doi.org/103109/1061186X2011622404 [Internet]. 2011 Dec [cited 2023 Jun 9];19(10):900–14. Available from: https://www.tandfonline.com/doi/abs/10.3109/1061186X.2011.622404

11. Roa WH, Azarmi S, Al-Hallak MHDK, Finlay WH, Magliocco AM, Löbenberg R. Inhalable nanoparticles, a non-invasive approach to treat lung cancer in a mouse model. J Control Release. 2011 Feb 28;150(1):49–55.

12. Feng Y, Chen X, Yang M. An In Silico Investigation of a Lobe-Specific Targeted Pulmonary Drug Delivery Method. Front Biomed Devices, BIOMED - 2018 Des Med Devices Conf DMD 2018 [Internet]. 2018 Jun 14 [cited 2023 Apr 28]; Available from: /BIOMED/proceedings-abstract/DMD2018/40789/271913

13. Islam MR, Feng Y. Achieving Targeted Delivery of Chemotherapeutic Particles to Small Airway Tumors via Pulmonary Route Using Endotracheal Catheters: A CFPD Study. Pharm 2023, Vol 16, Page 158 [Internet]. 2023 Jan 22 [cited 2023 Apr 28];16(2):158. Available from: https://www.mdpi.com/1424-8247/16/2/158/htm

14. Gürzing S, Thiebes AL, Cornelissen CG, Jockenhoevel S, Reddemann MA. Suitability of Bronchoscopic Spraying for Fluid Deposition in Lower Airway Regions: Fluorescence Analysis on a Transparent In Vitro Airway Model. J Aerosol Med Pulm Drug Deliv [Internet]. 2022 Oct 1 [cited 2023 Jun 9];35(5):269–77. Available from: https://www.liebertpub.com/doi/10.1089/jamp.2022.0016

15. Haas CF, Eakin RM, Konkle MA, Blank R. Endotracheal Tubes: Old and NewDiscussion. Respir Care [Internet]. 2014 Jun 1 [cited 2023 Jun 9];59(6):933–55. Available from: https://rc.rcjournal.com/content/59/6/933

16. Rhein T Van, Alzahrany · Mohammed, Banerjee · Arindam, Salzman · Gary. Fluid flow and particle transport in mechanically ventilated airways. Part I. Fluid flow structures. Med Biol Eng Comput. 2016;54:1085–96.

17. Valenza F, Chevallard G, Fossali T, Salice V, Pizzocri M, Gattinoni L. Management of mechanical ventilation during laparoscopic surgery. Best Pract Res Clin Anaesthesiol. 2010 Jun 1;24(2):227–41.

18. Bayram B, Şancı E. Invasive mechanical ventilation in the emergency department. Turkish J Emerg Med. 2019 Apr 1;19(2):43–52.

19. Kleinstreuer C, Zhang Z. Airflow and Particle Transport in the Human Respiratory System. https://doi.org/101146/annurev-fluid-121108-145453 [Internet]. 2009 Dec 21 [cited 2023 Apr 28];42:301–34. Available from: https://www.annualreviews.org/doi/abs/10.1146/annurev-fluid-121108-145453

20. Alzahrany M, Van Rhein T, Banerjee A, Salzman G. Fluid flow and particle transport in mechanically ventilated airways. Part II: particle transport. Med Biol Eng Comput. 2016;54(7).

21. Lai Y, Wang X, Zhou K, Su J, Che G. The Feasibility and Safety of No Placement of Urinary Catheter Following Lung Cancer Surgery: A Retrospective Cohort Study With 2,495 Cases. https://doi.org/101080/0894193920191663377 [Internet]. 2019 [cited 2023 Jun 9];34(6):568–74. Available from: https://www.tandfonline.com/doi/abs/10.1080/08941939.2019.1663377

22. Ren Kang J, Hai Long L, Wen Yan S, Wei Wei W, Zhi Jun H, Chen W. Peripherally Inserted Central Catheter-Related Vein Thrombosis in Patients With Lung Cancer.

23. Khoa ND, Li S, Phuong NL, Kuga K, Yabuuchi H, Kan-O K, et al. Computational fluid-particle dynamics modeling of ultrafine to coarse particles deposition in the human respiratory system, down to the terminal bronchiole. Comput Methods Programs Biomed. 2023 Jul 1;237:107589.

24. Ostrovski Y, Dorfman S, Mezhericher M, Kassinos S, Sznitman J. Targeted Drug Delivery to Upper Airways Using a Pulsed Aerosol Bolus and Inhaled Volume Tracking Method. Flow, Turbul Combust [Internet]. 2019 Jan 15 [cited 2023 Jun 9];102(1):73–87. Available from: https://link.springer.com/article/10.1007/s10494-018-9927-1

25. Martonen TB, Guan X. Effects of tumors on inhaled pharmacologic drugs: I. Flow patterns. Cell Biochem Biophys [Internet]. 2001 [cited 2023 Jun 9];35(3):233–43. Available from: https://link.springer.com/article/10.1385/CBB:35:3:233

26. Srivastav VK, Kumar A, Shukla SK, Paul AR, Bhatt AD, Jain A. Airflow and Aerosol-Drug Delivery in a CT Scan based Human Respiratory Tract with Tumor using CFD. J Appl Fluid Mech [Internet]. 2014 Apr 1 [cited 2023 Jun 9];7(2):345–56. Available from: https://www.jafmonline.net/article_1448.html

27. Clinical Application of Mechanical Ventilation - David W. Chang - Google 图书 [Internet]. [cited 2023 Jun 9]. Available from: https://books.google.co.jp/books?hl=zh-CN&lr=&id=2egWAAAAQBAJ&oi=fnd&pg=PP1&dq=mechanical+ventilator+waveform&ots=6TV51FgkK2&sig=fEYo7K4tM9ppIshUieJLfT5YjbY&redir_esc=y#v=onepage&q=mechanical ventilator waveform&f=false

28. Alqahtani JS, AlAhmari MD, Alshamrani KH, Alshehri AM, Althumayri MA, Ghazwani AA, et al. Patient-Ventilator Asynchrony in Critical Care Settings: National Outcomes of Ventilator Waveform Analysis. Hear Lung. 2020 Sep 1;49(5):630–6.

29. Finfer SR, Vincent J-L, Slutsky AS, Ranieri VM. Ventilator-Induced Lung Injury. https://doi.org/101056/NEJMra1208707 [Internet]. 2013 Nov 28 [cited 2023 Jun 9];369(22):2126–36. Available from: https://www.nejm.org/doi/full/10.1056/NEJMra1208707

30. Mutuku JK, Hou WC, Chen WH. An Overview of Experiments and Numerical Simulations on Airflow and Aerosols Deposition in Human Airways and the Role of Bioaerosol Motion in COVID-19 Transmission. Aerosol Air Qual Res [Internet]. 2020 [cited 2023 Jun 11];20(6):1172–96. Available from: https://aaqr.org/articles/aaqr-20-04-covid-0185

31. Weibel ER. Morphometry of the Human Lung. Morphometry Hum Lung. 1963;

32. Shelley DA, Sih BL, Ng LJ. An integrated physiology model to study regional lung damage effects and the physiologic response. Theor Biol Med Model. 2014;11(1).

33. Cohen BS, Lippmann M. Ultrafine Particle Deposition in a Human Tracheobronchial Cast. http://dx.doi.org/101080/02786829008959418 [Internet]. 2007 Jan 1 [cited 2023 May 6];12(4):1082–91. Available from: https://www.tandfonline.com/doi/abs/10.1080/02786829008959418

34. Koullapis P, Kassinos SC, Muela J, Perez-Segarra C, Rigola J, Lehmkuhl O, et al. Regional aerosol deposition in the human airways: The SimInhale benchmark case and a critical assessment of in silico methods. Eur J Pharm Sci. 2018 Feb 15;113:77–94.

35. Phuong NL, Ito K. Investigation of flow pattern in upper human airway including oral and nasal inhalation by PIV and CFD. Build Environ. 2015 Dec 1;94:504–15.

36. Lu Phuong N, Dang Khoa N, Inthavong K, Ito K. Particle and inhalation exposure in human and monkey computational airway models. https://doi.org/101080/0895837820181545810 [Internet]. 2019 Oct 15 [cited 2023 May 5];30(11–12):416–28. Available from: https://www.tandfonline.com/doi/abs/10.1080/08958378.2018.1545810

37. Phuong NL, Khoa ND, Ito K. Comparative numerical simulation of inhaled particle dispersion in upper human airway to analyse intersubject differences. https://doi.org/101177/1420326X19894128 [Internet]. 2020 Jan 8 [cited 2023 May 5];29(6):793–809. Available from: https://journals.sagepub.com/doi/abs/10.1177/1420326X19894128?journalCode=ibeb

38. Nagano H, Kato S, Zhu S, Ozeki Y, Matsunaga K, Kataoka T. Ventilation Characteristics of Modeled Compact Car Part 2 Estimation of Local Ventilation Efficiency and Inhaled Air Quality. SAE Int J Passeng Cars - Mech Syst [Internet]. 2008 Apr 14 [cited 2023 Jun 11];1(1):623–30. Available from: https://www.sae.org/publications/technical-papers/content/2008-01-0731/

39. Stahlhofen W, Gebhart J, Heyder J. Experimental determination of the regional deposition of aerosol particles in the human respiratory tract. http://dx.doi.org/101080/15298668091424933 [Internet]. 2010 Jun 1 [cited 2023 Jul 9];41(6):385-398a. Available from: https://www.tandfonline.com/doi/abs/10.1080/15298668091424933

40. Chan TL, Lippmann M. Experimental measurements and empirical modelling of the regional deposition of inhaled particles in humans. http://dx.doi.org/101080/15298668091424942 [Internet]. 2010 Jun 1 [cited 2023 Jul 9];41(6):399–409. Available from: https://www.tandfonline.com/doi/abs/10.1080/15298668091424942

41. Asgharian B, Hofmann W, Bergmann R. Particle deposition in a multiple-path model of the human lung. Aerosol Sci Technol [Internet]. 2001 [cited 2023 Jul 9];34(4):332–9. Available from: https://www.tandfonline.com/action/journalInformation?journalCode=uast20

42. Asgharian B, Price O, Borojeni AAT, Kuprat AP, Colby S, Singh RK, et al. Influence of Alveolar Mixing and Multiple Breaths of Aerosol Intake on Particle Deposition in the Human Lungs. SSRN Electron J [Internet]. 2022 Feb 25 [cited 2023 Jul 9]; Available from: https://papers.ssrn.com/abstract=4042662

43. Deng Q, Deng L, Miao Y, Guo X, Li Y. Particle deposition in the human lung: Health implications of particulate matter from different sources. Environ Res. 2019 Feb 1;169:237–45.

44. Hammer T, Fissan H, Wang J. Determination of the delivered dose of nanoparticles in the trachea-bronchial and alveolar regions of the lung. NanoImpact. 2019 Feb 1;14:100162.

45. Islam MS, Saha SC, Sauret E, Gemci T, Gu YT. Pulmonary aerosol transport and deposition analysis in upper 17 generations of the human respiratory tract. J Aerosol Sci. 2017 Jun 1;108:29–43.

Acknowledgement

I am profoundly grateful for the unwavering support and guidance of my esteemed supervisor, Professor Ito. Throughout the entire research journey, his boundless kindness, illuminating guidance, and vast reservoir of knowledge have been indispensable in the successful completion of this project. From the very inception of the study to its culmination, Professor Ito's mentorship has been nothing short of transformative. Under Professor Ito's expert guidance, I have been fortunate to receive invaluable insights and direction, which have played a pivotal role in shaping the trajectory of my research. His deep expertise and passion for the subject have not only inspired me but have also encouraged me to push the boundaries of my understanding and explore new avenues in my field. Whenever I encountered complex challenges or roadblocks, Professor Ito's unwavering support and encouragement provided the motivation and confidence needed to persevere. Beyond his academic expertise, Professor Ito's nurturing approach to mentorship has created an environment of trust and mutual respect. He took the time to understand my strengths and weaknesses, fostering an atmosphere that allowed me to thrive and grow. The constructive feedback and insightful suggestions he provided were invaluable in refining my research, and I am truly grateful for the personal attention and care he invested in my academic development. Professor Ito's mentorship extended beyond the realm of academia. He was not just a supervisor but also a source of guidance and support in various aspects of life. His wisdom and experiences served as a compass in navigating the challenges of both academic and personal life, imparting valuable life lessons that I will carry with me throughout my life.

I also wish to express my heartfelt appreciation to all the professors who have imparted their wisdom and insights during lectures, and to the warm-hearted teachers who have played instrumental roles in my academic journey. Their dedication to imparting knowledge and their commitment to nurturing young minds have been a constant source of motivation and inspiration for me. The invaluable lessons I have

learned from them have not only shaped my academic pursuits but have also influenced my personal growth, equipping me with essential skills and knowledge to face the challenges of life.

To my parents, I offer heartfelt thanks for their boundless love, unwavering support, and constant encouragement throughout my academic journey. Their belief in my abilities and their unwavering commitment to my success have been the driving force behind my perseverance and dedication. Their sacrifices, encouragement, and presence have been a pillar of strength, providing me with the courage and confidence to pursue my dreams. I am forever grateful to have a loving family to turn to, and I recognize that their unwavering support has been the foundation of my achievements.

My sincere appreciation also goes to my friends, whose unwavering belief in my abilities and constant words of encouragement have been a source of motivation during challenging times. Their camaraderie and support have made every step of this journey more enjoyable and meaningful, and I cherish the memories we have created together.

Lastly, I would like to express my profound gratitude to all those who have devoted their time to reading this thesis and offering valuable advice and feedback. Your contributions have enriched the quality of this work and have not gone unnoticed. The diverse perspectives and constructive criticisms provided by the readers have helped shape this research into its current form, and I am truly grateful for your valuable input.

In conclusion, I am overwhelmed with gratitude for the unwavering support and guidance I have received from various individuals throughout this academic journey. From the inspiring mentorship of Professor Ito to the encouragement and support from professors, teachers, parents, and friends, each one of them has played a vital role in shaping my academic and personal growth. Their contributions have been the bedrock of this research endeavor, and I recognize that without their belief in me, this achievement would not have been possible. As I embark on new academic endeavors and challenges, I carry with me the invaluable lessons and support I have received, and I am eager to make a positive impact in my field and contribute to society with the knowledge and skills I have acquired.